DISSERTATIONES
PHYSICAE
UNIVERSITATIS
TARTUENSIS
**110**

MAREK OJA

# Investigation of nano-size α- and transition alumina by means of VUV and cathodoluminescence spectroscopy

DISSERTATIONES PHYSICAE UNIVERSITATIS TARTUENSIS
**110**

DISSERTATIONES PHYSICAE UNIVERSITATIS TARTUENSIS
**110**

**MAREK OJA**

# Investigation of nano-size α- and transition alumina by means of VUV and cathodoluminescence spectroscopy

UNIVERSITY OF TARTU
Press

This study was carried out at the Institute of Physics, University of Tartu, Estonia.

The dissertation was admitted on April 4, 2017, in partial fulfilment of the requirements for the degree of Doctor of Philosophy in physics and was allowed for defence by the Scientific Council of the Institute of Physics, University of Tartu.

Supervisors: Dr. Marco Kirm
Institute Physics, University of Tartu, Estonia

Dr. Eduard Feldbach
Institute Physics, University of Tartu, Estonia

Opponent: Dr. Stéphane Guizard
Ecole Polytechnique, France

Defence: May 22, 2017, at University of Tartu, Estonia



ISSN 1406-0647
ISBN 978-9949-77-415-9 (print)
ISBN 978-9949-77-416-6 (pdf)



University of Tartu Press
www.tyk.ee

# CONTENTS

LIST OF PUBLICATIONS INCLUDED IN THE THESIS ..... 6

LIST OF ABBREVIATIONS ..... 7

1. INTRODUCTION ..... 8

2. GENERAL AND STRUCTURAL PROPERTIES OF ALUMINA ..... 10

3. ELECTRONIC AND LUMINESCENCE PROPERTIES OF ALUMINA ..... 13

4. EXPERIMENTAL SETUPS FOR LUMINESCENCE STUDIES ..... 17

5. SYNTHESIS OF ALUMINA NANOPOWDERS ..... 22

6. CHARACTERISATION OF OBTAINED ALUMINAS ..... 24

7. LUMINESCENCE STUDIES OF MIXED TRANSITION ALUMINA . 29
   7.1 Intrinsic absorption onset of different alumina nanopowders ..... 29
   7.2 Intrinsic luminescence in the UV and VUV range ..... 32
   7.3 Defect luminescence in aluminas ..... 37
   7.4 Impurity luminescence of alumina powders ..... 42

8. DIAGNOSTICS OF ODS STEELS FOR HEAVY IRRADIATION ENVIRONMENT ..... 46

9. SUMMARY ..... 49

10. SUMMARY IN ESTONIAN ..... 50

11. ACKNOWLEDGEMENTS ..... 51

12. REFERENCES ..... 52

13. PUBLICATIONS ..... 57

CURRICULUM VITAE ..... 79

ELULOOKIRJELDUS ..... 82

## LIST OF PUBLICATIONS INCLUDED IN THE THESIS

**I** M. Kirm, E. Feldbach, A. Kotlov, P. Liblik, A. Lushchik, **M. Oja**, E. Palcevskis, VUV spectroscopy and electronic excitations in nano-size alumina, *Radiation Measurements*, **45** (2010) 618–620.

**II** **M. Oja**, E. Feldbach, A. Kotlov, H. Mändar, S. Vielhauer and M. Kirm, Intrinsic and Extrinsic Luminescence of Nanosize Transition Alumina Powders, *Radiation Measurements* **56** (2013) 411–414.

**III** **M. Oja**, E. Tõldsepp, E. Feldbach, H. Mägi, S. Omelkov, M. Kirm, Luminescence Study of Alumina Nanopowders Prepared by Various Methods, *Radiation Measurements* **90** (2016) 75–79.

## AUTHOR'S CONTRIBUTION

The author was responsible for luminescence measurements and data analysis of the results presented in papers **I–III**. The author prepared samples studied in papers **II** and **III**. The author characterised the samples studied in papers **I**, **II** and **III** using x-ray diffraction analyse and took part in SEM measurements. The author took part of writing paper **I** and was responsible for writing papers **II** and **III**.

## OTHER PUBLICATIONS OF THE DISSERTANT

1. E. Feldbach, T. Avarmaa, V. Denks, H. Mägi, **M. Oja**, E. Tõldsepp, M. Kirm, Tuning the electronic properties of naturally nanostructured compounds, *Physica Scripta*, **T157** (2013) 014013.

# LIST OF ABBREVIATIONS

| | |
|---|---|
| AFM | atomic force microscopy |
| ALD | atomic layer deposition |
| BET | Brunaur-Emmet-Teller |
| CL | cathodoluminescence |
| CT | charge transfer |
| DFT | density functional theory |
| e-h pairs | electron-hole pairs |
| EPR | electron paramagnetic resonance |
| IR | infrared |
| LTW | long-time window |
| ODS | oxide dispersion-strengthened |
| PL | photoluminescence |
| RT | room temperature |
| SEM | scanning electron microscopy |
| SR | synchrotron radiation |
| SSA | specific surface area |
| STE | self-trapped exciton |
| STW | short-time window |
| TEM | transmission electron microscopy |
| TI | time-integrated |
| VUV | vacuum ultraviolet |
| XPS | X-ray photoelectron spectroscopy |
| XRD | X-ray diffraction |
| XUV | extreme ultraviolet |

# 1. INTRODUCTION

Metal oxides are important materials in many areas of chemistry, materials science, and physics. Different metal oxides can be used in the fabrication of microelectronic circuits, sensors, piezoelectric devices, fuel cells, coatings for the passivation of surfaces against corrosion, and as catalysts.

Nano-sized materials have gained a lot of attention due to changes in their properties and appearance if additional qualities as the size of the particles decrease. The size of particles affects the crystal structure stability, lattice symmetry, and unit cell parameters. Also, the particle size has an effect on electronic properties. A well-known example is the shift in absorption and photoluminescence to higher energy known as blue shift in semiconductor nanomaterials as the particle size decreases, this being due to quantum confinement effects (e.g. PbS nanoparticles [1]).

Aluminium oxide or alumina ($Al_2O_3$), which was studied in this work, has several unique properties attractive for numerous applications. Just to mention one – the transparency in deep UV in combination with high corrosion resistance and mechanical strength makes it useful as an optical material for harsh environment. In nature, aluminium oxide is widely found as a mineral called corundum. There are well-known aluminium oxide natural derivatives, rubies and sapphires, which are used in jewel industry. Ruby (aluminium oxide single crystal doped with $Cr^{3+}$) was also used as the first solid-state laser material [2].

When going from macroscopic aluminium oxide to micro- and nano-size powders then it is possible to synthesise metastable or transition alumina phases, which are not found as bulk materials. As the name transition implies, transition alumina phases are usually present during synthesis processes before the high-temperature treatment. Metastable phases are stable below certain temperatures and heating the material at higher temperatures we end up with thermodynamically stable $\alpha$-$Al_2O_3$. The main alumina metastable phases labelled as $\gamma$-, $\delta$-, $\theta$-, $\eta$- and $\kappa$-$Al_2O_3$ differ from each other due to their crystal structure. This difference in the crystal structure can give raise to different electronic properties in comparison with the thermodynamically stable $\alpha$-$Al_2O_3$ phase. Some of the properties of transition aluminas can be advantageous for certain applications, e.g. metastable $\gamma$-$Al_2O_3$ powder is used as a catalysts host material due to a high specific surface area.

Due to the fact that most of the metastable aluminas are not sufficiently studied by powerful optical methods (see section 3), the main goal of this research work was to investigate the electronic and optical properties of different alumina metastable phases ($\gamma$-, $\delta$-, and $\theta$-$Al_2O_3$) in comparison with the thermodynamically stable $\alpha$-$Al_2O_3$ phase.

The main aim of the work is to clarify:

- Electronic properties, nature and relaxation processes of electronic excitations in transition alumina.

- Influence of (nano)size effects on electronic and optical properties of transition and α-alumina.

In order to achieve goals set, the specific subtasks were performed:

1. Synthesis of the transition alumina samples and their characterisation.
2. Time-resolved luminescence spectroscopy study at low temperatures under electron beam and VUV-XUV synchrotron radiation excitation.
3. Experimental determination of band gap values and relevant properties of electronic excitations for different alumina metastable phases.
4. Investigation of phase composition and crystallite size related specific features in luminescence of alumina samples prepared with different synthesis methods.
5. Analysis of the nature of revealed luminescence bands of intrinsic and extrinsic origin in different alumina phases.

# 2. GENERAL AND STRUCTURAL PROPERTIES OF ALUMINA

In nature, aluminium oxide is usually found as a mineral called corundum, which is a crystalline form of α-alumina. Corundum can contain a variety of impurity ions which colour the corundum crystals. The best-known varieties of corundum crystals are red-coloured chromium impurity containing rubies and blue-coloured iron and titanium impurities containing sapphires. Corundum has an extreme hardness which makes it useful to use as an abrasive material and suitable for use in harsh working conditions. At Mohs hardness scale, it has a value of nine [3].

**Structure**

Besides the thermodynamically stable alumina phase α-$Al_2O_3$ there are different metastable polymorphs (e.g. δ, θ, γ, κ, η, λ etc.), which all have different crystal structures. Only crystal structures of investigated phases (α, γ, δ and θ) will be discussed in this work. Thermodynamically stable α-$Al_2O_3$ has trigonal symmetry with space group R-3c (No. 167). The structure of α-$Al_2O_3$ is presented in Figure 1a. Oxygen atoms in α-$Al_2O_3$ structure can be considered to form a hexagonal close-packed (hcp) sublattice with 2/3 interstices filled with aluminium cations in an ordered array [4]. The hexagonal parameters for α-$Al_2O_3$ are c = 1.297 nm and a = 0.475 nm [4]. Metastable alumina structures are not well known as there are no single crystals which are suitable for a standard structure analysis. Quite often metastable alumina crystallites have nano-size, thus prohibiting exact identification of their structures due to XRD line broadening.

Alumina α-phase has melting point of 2327 K, boiling point of 3250 K and a relatively high density of 3.99 g/cm$^3$ [3]. As other alumina phases transit to α-$Al_2O_3$ at temperatures below its melting point then there are no data on boiling and melting points for other alumina phases. The value for density (3.97 g/cm$^3$) is known only for γ-$Al_2O_3$ [3].

Metastable alumina structures can be divided into two broad categories which have either a face-centred cubic (fcc) or hexagonal close packed (hcp) packing of anions [5]. Alumina polymorphs with fcc packing of oxygen are δ, θ, γ, and η phases and polymorphs with hcp packing are κ- and χ-$Al_2O_3$.

γ-$Al_2O_3$ has been described as a defect spinel structure with space group Fd3m and idealised formula $Al_{21+1/3}\square_{2+2/3}O_{32}$ (□ denotes a vacancy) [4, 6]. In α-$Al_2O_3$ cations occupy only octahedrally coordinated interstitial sites forming $AlO_6$ units but in γ-$Al_2O_3$ about 25–30% cations occupy also tetrahedrally coordinated interstitial sites ($AlO_4$ units) and cation vacancies are distributed randomly over tetrahedral sites [4, 7]. In recent years, other structures were proposed for γ-$Al_2O_3$ as well. There have been propositions that γ-$Al_2O_3$ possesses a low symmetry tetragonal structure with space group $I4_1/amd$ [8,9]. The crystal structure of γ-$Al_2O_3$ has been an object of debate for years and still it is not firmly established as the crystallite size is small and lines on a diffractogram are broad for γ-$Al_2O_3$.

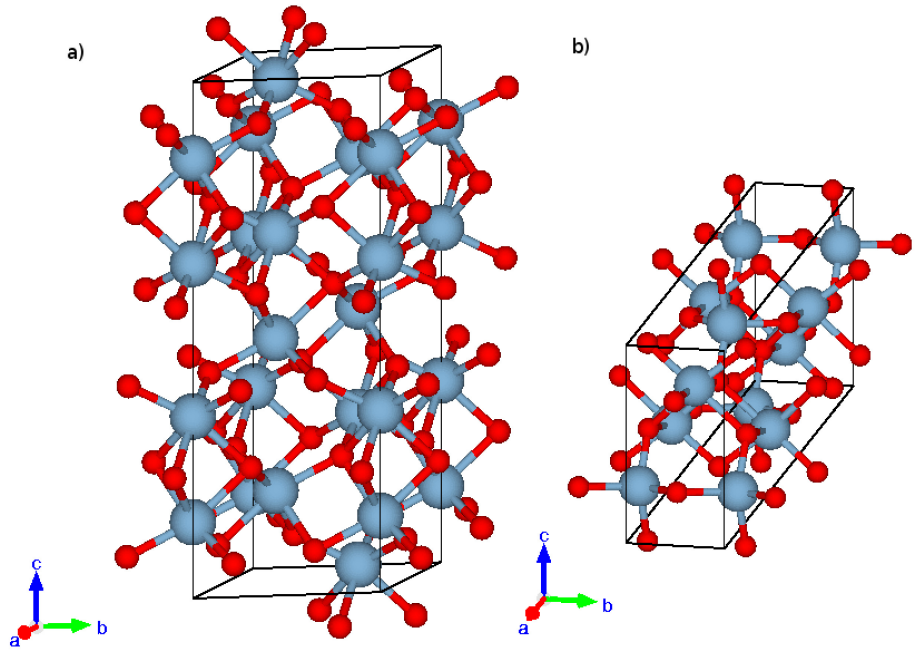


**Figure 1.** Crystal structure of α-$Al_2O_3$ (a) [10] and θ-$Al_2O_3$ (b) [11]. Aluminium ions designated as blue and oxygen ions as red spheres, respectively.

δ- and θ-$Al_2O_3$ have gathered less attention than γ-$Al_2O_3$ mainly due to difficulties in synthesising phase-pure samples. δ-$Al_2O_3$ has a superlattice of the spinel structure with ordered cation vacancies [4]. There have been proposed two different unit cells for δ-$Al_2O_3$ – tetragonal or orthorhombic [4]. The two different unit cells were identified from samples produced using different synthesis procedures. Newer results by Kovarik et al. [7] show that in δ-$Al_2O_3$ there is intergrowth of two closely related crystallographic variants. It was revealed that this intergrowth structure lacks a long-range periodicity along one principal direction. The intergrown structures have orthorhombic and monoclinic symmetry, respectively. 37.5% of cations occupy tetrahedral sites and 62.5% are located at octahedral sites according to Kovarik et al. [7].

θ-$Al_2O_3$ possesses monoclinic symmetry and the structure is isomorphous to β-$Ga_2O_3$ [4]. The structure of θ-$Al_2O_3$ is presented in Figure 1b. Later studies by Kovarik et al. [12] have shown that θ-$Al_2O_3$ can be also interpreted as intergrowth of two crystallographic variants with monoclinic symmetry. One of these crystallographic variants is structure isomorphous to β-$Ga_2O_3$ and the second one similar to one of the structures identified for δ-$Al_2O_3$ [12]. Both these structures have previously separately assigned as θ-$Al_2O_3$ structure [4] but actually, these are intergrowth of both structures [12]. Possibly the ratio of both crystallographic phases in obtained compounds depends on the synthesis procedure. In structures isomorphous to β-$Ga_2O_3$ the cations are equally divided

between octahedral and tetrahedral sites [4, 12]. In the second structure, similar to δ-$Al_2O_3$, cations are substituted to tetrahedral and octahedral sites in a ratio 32.5% and 67.5%, respectively [12].

In summary, the polymorph with the largest occupation ratio of cations at tetrahedral/octahedral sites is for θ-$Al_2O_3$ and this ratio decreases in the row δ-, γ- and α-$Al_2O_3$, where cations are located only in octahedral sites. Also, alumina's metastable polymorphs have lower symmetry and more vacancies are present in the structure. From this, one can expect rather different luminescence properties in transition alumina due to intrinsic (incl. excitonic) and extrinsic excitations.

**Phase stability**

The stability of alumina polymorphs also depends on the crystallite size. Theoretical studies have shown that the γ-$Al_2O_3$ is energetically more stable when it has higher specific surface area compared to that of α-$Al_2O_3$. The latter one is stable with specific surface area values below 125 $m^2/g$ [13]. This means that it is more difficult to synthesise α-$Al_2O_3$ with small crystallite size.

The phase transition temperatures are not very well defined for alumina polymorphs. The transition can occur in a range of temperatures depending on the synthesis method and starting material. In Figure 2 the transition temperatures for some synthesis processes, collected by Levin and Brandon, are shown [4]. These temperatures and formation of intermediate phases vary a large extent depending on the precursor materials and selected synthesis route. At the highest temperatures, the final product is always α-$Al_2O_3$.

To conclude, a rich family of transition aluminas is a real challenge for experimental investigation because of coexistence of different phases and variety of crystallographic structures. There is no doubt that electronic properties are different due to the varying occupation of cation sites, the amount of vacancies and complicated structure. Adding influence of crystallite size will extend the complexity of research task.

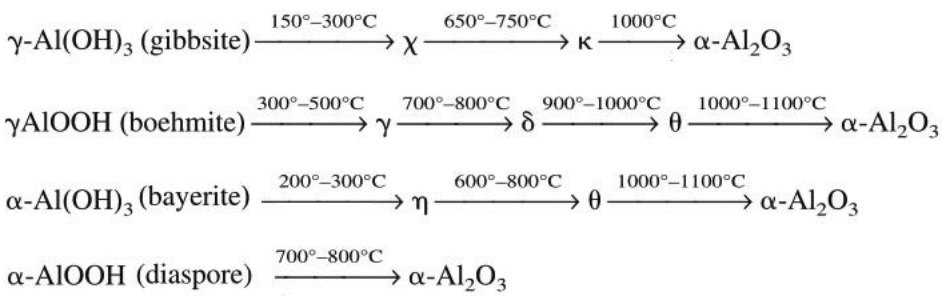


**Figure 2.** Phase transition temperatures of metastable aluminas for some synthesis routes (adapted from [4]).

# 3. ELECTRONIC AND LUMINESCENCE PROPERTIES OF ALUMINA

Electronic properties of materials can be studied using multiple experimental and theoretical methods. Electron spectroscopy methods in all variations are widely used in studies of electronic properties of condensed matter. However, for bulk insulators, it is not so suited because of sample charging effects and high surface sensitivity. Therefore, photon-in and photon-out techniques like luminescence, Raman spectroscopy, reflection and absorption spectroscopy are the main spectroscopic methods. Also, different theoretical methods have been used to calculate the electronic properties of materials (e.g. based on density functional theory [14–16]). With the help of luminescence spectroscopy, the band gap value can be determined and possible electronic states within the gap due to defects and impurities can be identified. Band (energy) gap is defined as the energy region between the top of the valence band and the bottom of conduction band where no electron states exist in pure, defect- and impurity-free material. Sharp increase in luminescence excitation efficiency is observable due to strong absorption at excitation energies larger than the band gap value when electrons are excited from the valence band to the conduction band and produce free mobile electron-hole pairs. The energy absorbed in a solid can be released either radiatively as intrinsic (excitonic) or recombinational (at a defect or impurity centre) luminescence or non-radiatively forming transient or stable defects. Free electron-hole pairs can be self-trapped leading to the formation of self-trapped holes, excitons or even electrons. Self-trapped exciton (STE) is a bound electron-hole pair, where either electron or hole is trapped in a potential well due to self-induced lattice distortion [17]. Modelling various (self-trapping in a perfect lattice, trapping at defects and impurities) electron and hole trapping processes in oxides (incl. nanomaterials) is a very active research topic [18].

**Intrinsic absorption and luminescence of STEs and defects**

Electronic and optical properties of α-$Al_2O_3$ are rather well studied by various authors and is thoroughly summarised in an overview publication by Valbis and Itoh [19]. Due to alumina's relevance in various applications (e.g. [20–22]) and interest in fundamental aspects of relaxation of electronic excitations (e.g. [23–26]) the studies of its properties have been continued intensively.

The experimentally determined and theoretically estimated band gap values for different alumina phases are shown in Table 1. The band gap of α-$Al_2O_3$ equals to 9.4 eV ([23] and references therein). In reality, the intrinsic absorption for α-$Al_2O_3$ starts at 8.85 eV because of the absorption band of $p^5s$ excitons between 8.85 eV and 9.4 eV [23]. After self-trapping two kind of singlet STEs are formed with emission bands peaked at 7.6 and 3.77 eV, respectively. The former one is only well excited in the narrow region of long wavelength excitonic absorption 8.85 – 9.1 eV, whereas the latter one reaches maximum at 9.2 eV and is well excited in the region of interband transitions above 9.4 eV.

The decay time of the 7.6 eV STE emission is either 7 or 22 ns under excitation in excitonic or interband transition region, respectively [27, 28]. For $Al_2O_3$ single crystal, the decay times under XUV excitation (150 eV photons) are 1.05, 7.1 and 53.7 ns, which shows that the decay kinetics can be complicated due to a very high excitation energy compared to direct intra-centre excitation [29]. The 3.7 eV STE has decay time in ns range [19, 23]. For γ-$Al_2O_3$ and θ-$Al_2O_3$ the onset of intrinsic absorption was not previously reported and in our research, we found the respective values to be equal to 7.0 eV and 7.5 eV, respectively (Paper I, II and section 7.1 of this work). Later Museur et. al. [30] obtained similar values for γ-$Al_2O_3$ and θ-$Al_2O_3$ (Table 1). Kirm et al. [31] have ascribed excitation onset at 7.2 eV to the intrinsic absorption of $AlO_4$ cells in δ-$Al_2O_3$. In thin films, intrinsic absorption starts at ~7.2 eV for crystalline films and ~6.6 eV for amorphous samples [20]. These films grown by atomic layer deposition (ALD) were composed of different alumina phases. According to the aforementioned studies, this enables to conclude that the onset of intrinsic absorption in transition aluminas shifts to lower energies in comparison to α-$Al_2O_3$ and one could expect that excitonic absorption and STE emission follow similar trends.

Defects are imperfections in the crystal lattice as side effects of any synthesis process or can be introduced while exposing to irradiation by ionising radiation or energetic particles. The most well-known defects for α-alumina are F and $F^+$ defect centres. The F-centre is oxygen vacancy with two electrons and $F^+$-centre is oxygen vacancy with one electron localised at the vacancy. The F-centre has emission at 3.0 eV with a long decay time of 36 ms [19, 24]. The main F-centre absorption band is at 6.1 eV [32]. The $F^+$-centre has emission peaked at 3.8 eV with a short decay of 2.1 ns [24, 33]. $F^+$-centre has multiple absorption bands at 4.8 eV, 5.4 eV and 6 eV [27, 32]. Another possible defect centre is $F_2$-centre which consists of oxygen divacancy with four electrons. It has emission with a maximum at 2.4 eV (decay of 50 or 68 ms) and absorption band at 4.1 eV [32, 34]. Also, $Al_i^+$-centre, which consist of an interstitial aluminium ion having the charge of +1, has been found in α-$Al_2O_3$ with emission at 2.4 eV and decay of 56 μs [35, 36].

**Transition aluminas**

For transition aluminas, experimental investigations have been performed for γ-$Al_2O_3$ [30,37], δ-$Al_2O_3$ [31], θ-$Al_2O_3$ [30] and κ-$Al_2O_3$ [38].

κ-$Al_2O_3$ has not been practically studied by luminescence methods and at room temperature (RT) only single unidentified band at 5.6 eV has been recorded in cathodoluminescence study [38]. No band gap value has been determined for κ-$Al_2O_3$ to our best knowledge. However, the high-energy onset of this emission band suggests that the energy gap has to be 6.5 eV or higher.

For γ-$Al_2O_3$ emission band at 3.6 eV was revealed at RT and attributed to $F^+$-centre [37,38]. In γ-$Al_2O_3$ there has been found the F- and $F_2$-centre emission at 3.0 and 2.4 eV, respectively [39], which coincide with the respective spectral positions of these centres in α-$Al_2O_3$.

Mixed phase $Al_2O_3$ samples, a typical situation in transition alumina research, have been investigated by various authors [26, 40–42]. In δ-$Al_2O_3$ and γ-$Al_2O_3$ mixture there have been identified F- and $F^+$-centre at 3 eV and 3.8 eV, respectively, and the emission band at 3.4 eV, which was proposed to be $F_s$ – surface F-centre [41]. The F- and $F^+$-centre spectral positions coincide with those in α-$Al_2O_3$. Gorbunov et al. [42] proposed $F^+_s$-centre in a mixture of δ-$Al_2O_3$ and γ-$Al_2O_3$ with the emission energy of 3.2 eV.

Museur et al. [30] found an emission band at 2.9 eV with two decay components in three different alumina phases, α-, γ- and θ-$Al_2O_3$, and according to literature three different interpretations were suggested as emission from F-centre (long decay), $F^+_s$-centre (short decay) or V-centres (negatively charged cation vacancies able to trap holes with a positive charge). Also in the same work, up to three different STEs were revealed and their luminescence data is presented in Table 1.

**Impurity ions**

3d elements are common impurities in aluminas showing their typical luminescence. The most well-known impurity $Cr^{3+}$ ion emits in the red spectral region and the emission lines are recognised as R-lines. The R-lines designate the $^2E \rightarrow {}^4A_2$ transition of $Cr^{3+}d^3$ configuration. In α-alumina, these lines are at 694.3 and 692.9 nm [2]. The $Cr^{3+}$ luminescence centre has been widely studied in alumina [22, 25, 43–47]. In θ-$Al_2O_3$ $Cr^{3+}$ R-lines are shifted to 682.6 nm and 685.9 nm [21, 48, 49]. In γ-$Al_2O_3$ there have not been observed narrow R-lines, but instead a broad line around 700 nm, which is due to inhomogeneous broadening [48]. Other optically active impurities are for example $Ti^{3+}$, $Fe^{3+}$, $Mn^{2+}$ etc. α-$Al_2O_3$ crystal doped with $Ti^{3+}$ has a broad luminescence band with maxima at 700 nm, which is due to the transition between the $^2E_g$ and $^2T_{2g}$ manifolds [50]. $Al_2O_3$ doped with $Ti^{3+}$ is used as tuneable solid state laser [51]. $Mn^{2+}$ luminescence centre has emission at 600 nm and $Mn^{4+}$ centre at 676 nm having a weak vibronic structure [52]. $Fe^{3+}$ ion transition $^4T_1 \rightarrow {}^6A_1$ emission is proposed to be around 750 nm for nano-size alumina [40]. Instead of pure $Fe^{3+}$ luminescence Snytnikov et al. have proposed the broad luminescence at 750 nm is due to interaction between $Cr^{3+}$ and $Fe^{3+}$ impurity ions in alumina [21].

**Theoretical calculations**

Theoretical calculation for optical properties have been made for α-, κ-, γ-, θ-$Al_2O_3$ [15], χ-, κ-, α-$Al_2O_3$ [53], γ- $Al_2O_3$ [54–56], α-, θ-$Al_2O_3$ [57]. According to these DFT calculations, the band gap value changes systematically in transition aluminas according to the following rule $\alpha > \kappa > \theta > \gamma$ with the calculated band gap values of 6.72 eV, 5.49 eV, 5.04 eV and 4.40 eV [15], respectively. Theoretical calculations result in smaller values than experimentally determined ones, as density functional theory does not describe excited states correctly. According to the theoretical studies, the general features of the density of states curves are similar for different alumina phases with two valence bands and a conduction band. The lower valence band consist of O 2s orbitals, the upper

valence band consist of mainly O 2p orbitals intermixed with Al 3s and Al 3p orbitals and the conduction band of O 2s and Al 3s with a small addition of O 2p characters [15, 57, 58]. Authors observe downshift of the conduction band, which is the reason of band gap reduction in metastable aluminas, this being due to occupation of Al atoms in tetrahedral sites [15, 57]. Another problem with the theoretical studies of metastable alumina polymorphs is that the exact structure of metastable alumina polymorphs is still questionable. There have been proposed multiple structures, but structural information is an important input for band structure calculations and any inconsistency results in scattered values.

As seen from Table 1 the electronic properties of α-$Al_2O_3$ are well-known contrary to transition aluminas where there is still a lot of missing experimental information, although considerable amount data were recorded during the last couple of years. Analysis of collected data will contribute to the formation of general understanding on optical and electronic properties of transition aluminas.

**Table 1.** Main electronic and luminescence properties for α-, γ-, δ-, and θ-$Al_2O_3$.

| Phase | $E_g$ (value or onset of intrinsic absorption) | | Intrinsic (STE) and extrinsic (defect) luminescence bands ant their life-times given in brackets |
|---|---|---|---|
| | Experimental | Theoretical | |
| α-phase | $E_g$ = 9.4 eV<br>absorption onset at 8.9 eV [23] | 6.72 eV [15]<br>6.24 [57] | STE: 7.6 eV (7 and 22 ns) [27] and 3.7 eV [19, 23]<br>F 3.0 eV (36 ms) [19, 24]<br>$F^+$ 3.8 eV (2.1 ns) [24, 32]<br>$F_2$ 2.4 eV (50 or 68 ms) [32, 34]<br>Nano-size:<br>STE 7.6, 5.2, 4.1 eV [30] |
| γ-phase | 6.85 eV [30] | 4.40 eV [15] | $F^+$ 3.6 eV [37, 38] or 3.8 eV [30]<br>$F_2$ 2.4 eV [39] |
| δ-phase | 7.2 eV [31] | | Two emission bands at 5 and 5.9 eV [31] |
| θ-phase | 7.6 eV [30] | 5.04 eV [15]<br>4.64 eV [57] | STE 6.0 eV, 4.5 eV and 4.2 eV [30]<br>$F^+$ 3.8 eV [30] |

# 4. EXPERIMENTAL SETUPS FOR LUMINESCENCE STUDIES

Synchrotron radiation (SR) has in many ways superior properties compared to experimental setups available in laboratories. It is very bright, polarised, pulsed and tuneable broadband light source extending from the infrared (IR) to the X-ray region. SR is electromagnetic radiation which is produced when charged particles move with acceleration. In the case of synchrotrons, the relativistic charged particles, electrons or positrons, are accelerated in a circular orbit and emit electromagnetic radiation in a broad spectral range from which photons covering 4 – 1000 eV were exploited in present work. Also, electron beam was used as excitation source as with electrons it is possible to create electronic excitations in broad energy range. But it is not a selective excitation source, which does not enable to choose exact excitation energy and to perform selective investigations as in the case of photons. Compared to SR cathodoluminescence (CL) allows studying luminescence centres with lower quantum yield. Also, the penetration depth of electrons is larger than that of photons in the case of near band-gap edge excitation (~10 nm for 10 eV photons, ~50 nm for 130 eV photons and ~500 nm for 10 keV e-beam) and therefore CL is not so surface sensitive method as photoexcitation in VUV-XUV range. Luminescence studies of this work were performed on different setups in Tartu under electron beam excitation and in Hamburg using VUV-XUV SR at temperatures from 4 to 300 K.

**Cathodoluminescence**

Low temperature cathodoluminescence (CL) studies were performed using the home-built setup in Tartu, which was recently upgraded. It consists of two separate analysing channels based on self-made VUV monochromator equipped with a Hamamatsu solar-blind photomultiplier R6836 covering 4–12 eV spectral region. The second channel has an ARC SpectraPro 2300i monochromator operating in UV-visible region with various gratings and detectors covering 1.5–6 eV spectral region [59]. The Princeton Instruments CCD detector in combination with the ARC SpectraPro 2300i monochromator allows registering high-resolution emission spectra. The excitation source is a pulsed electron gun (EGPS-3101 Kimball Physics) with tuneable electron energy (1–10 keV) and for the accumulation of decay curves, a multiscaler photon counter (MSA-300, Becker&Hickl GmbH) is exploited. Decay curves were registered in a mode with excitation pulse width of $\delta t$ = 100 ns and with an interval between successive pulses $\Delta t$ = 200 μs or 2 ms. The 10 keV electron beam energy was chosen to get the maximum possible penetration depth in order to maximise luminescence signal and minimise surface effects. For MgO, the penetration depth of electrons with energy of 10 keV is around 500 nm [59]. Some spectra were measured before the cathodoluminescence setup was upgraded. Before the latest upgrade, there was a different UV-visible monochromator (a double prism monochromator with a Hamamatsu H6240 photon-counting head) and steady beam electron gun in use. Before measurement, the samples were covered with

thin 3 nm Pt films to avoid surface charging under electron beam excitation. Emission spectra recorded with VUV monochromator were corrected to the transmission of the detection system.

**Experiments under synchrotron radiation**

In Hamburg experiments with SR were carried out at two different beamlines BW3 [60, 61] and I (SUPERLUMI setup) [62] in order to record photoluminescence emission and excitation spectra, and decay kinetics. Beamlines BW3 and I were located at DORIS III synchrotron in DESY (*Deutsches Elektronen-Synchrotron*) which was closed in 2012.

The SUPERLUMI setup covered 4 eV – 40 eV (300 nm – 30 nm) excitation energy range using two gratings coated with Al/$MgF_2$ and Pt. The technical information of primary and secondary monochromators available at the SUPERLUMI setup is presented in Table 2. The incident arm is equipped with a McPherson normal incidence monochromator of 2 m focal length. Typically, the bandwidth of 0.03 nm was used in the excitation arm. It was possible to apply either a quartz filter for the excitations energies below 6.5 eV or a $MgF_2$ filter for energies 6–10 eV to eliminate excitation by the second orders of Al-grating. The ARC SpectraPro 2300i monochromator equipped with either R6358P (Hamamatsu) photomultiplier, or liquid nitrogen cooled Princeton Instrument CCD-camera was exploited to register luminescence in the range of 1.5 eV to 6 eV. A unique high throughput secondary VUV monochromator (Pouey type) was used to register luminescence above 5 eV. The technical information on available detectors is presented in Tables 3 and 4. Sodium salicylate was applied to normalise photoluminescence excitation spectra to the same number of incident photons on the sample.

**Table 2**. Description of monochromators used at the SUPERLUMI setup [63, 64]

| Monochromator | Primary | Secondary | VUV |
|---|---|---|---|
| Type | McPherson NIM 15° | ARC SpectraPro 308i Czerny-Turner | Pouey 28° |
| Aperture | f:20 | f:4 | f:2.8 |
| Focal length (mm) | 2000 | 300 | 500 |
| Grating size (mm) | Ø100 | 64x84 | 130x130 |
| Groove density (1/mm) | 1200 | 300/300/1200 | 1650 (variable) |
| Grating optimisation (nm) | 100(Al)/45(Pt) | 300/500/300 | |
| Linear dispersion (Å/mm) | 4 | 10.8/10.8/2.7 | 10 |
| Coating | Al+$MgF_2$ or Pt | Al | Al+$MgF_2$ |
| Working range of monochromators (nm) | Al-: 65-330 and Pt-grating: 30-330 | 190-1100 | 50-300 |

**Table 3**. Technical parameters and optical properties of photomultiplier and micro-sphere plate used at the SUPERLUMI setup [65]

| Detector | Hamamatsu R6358P Photomultiplier | El Mul E0344DTA1F microsphere plate detector |
|---|---|---|
| Working range (nm) | 185-830 | <180 |
| Cathode | LMA(multialkali) | CsI coating (1 μm) |
| Window | UV glass | |
| Amplifier gain | $3.5x10^6$ (-840V) | $5x10^6$ (-3.5 kV) |
| Time resolution | 1.4 ns | 320 ps |
| Dark pulses ($s^{-1}$) | 20 (RT) | 5..10 |
| Quantum efficiency (%) | 23 (530 nm) | |
| Typical voltage (V) | -840 | -3000…-3500 |

**Table 4.** Technical parameters of CCD detector used at the SUPERLUMI setup [64]

| Detector | Princeton Instruments |
|---|---|
| Number of Pixels | 1100x300 |
| Size of Pixel | 24x24μm |
| Working temperature | -118°C |
| Working range | 190-1100nm |

Beamline BW3 was a wiggler beamline, which operated in XUV i.e. “soft X-ray” spectral region [60] among other experiments providing photon beam for a mobile luminescence setup [61, 66]. It provided exciting photons in the energy range of 40 – 1800 eV, which covers core levels of Al 1s (~1560 eV), 2s (~118 eV), 2p (~72 eV) and oxygen 1s (~543 eV), 2s (~42 eV). The technical details of monochromators in operation and detectors are presented in Tables 5 and 6. The primary monochromator is SX-700 (Zeiss) with a planar grating with 6 m focal length. The designed spot size at the sample was 170 x 0.06 μm, in practice it depended on the beamline alignment and usually, it was a bit larger. The excitation energy was chosen to be 130 eV for most of the experiments as at this energy the maximum number of photons was available at BW3. The luminescence was recorded with a VUV monochromator operating in the range of 2.5 to 8.5 eV. The excitation spectra could not be corrected using sodium salicylate as the quantum yield of sodium salicylate changes under XUV radiation which degrades the performance of sodium salicylate through its damage leading to increase of non-radiative processes. At the beamline BW3 photon flux was continuously monitored via photocurrent from a gold mesh. Excitation spectra were finally corrected to the number of incident photons via recording calibrated photodiode current versus gold mesh signal as a function of excitation energy. Emission spectra were not corrected to the transmission of detection system because of the extremely wide energy range (2.5–8.5 eV) used in our studies.

**Table 5.** Description of monochromators in operation at BW3 beamline [66]

| Monochromator | Primary | Secondary |
|---|---|---|
| Monochromator type | SX-700 | VUV Seya-Namioka |
| Focal length (mm) | 6000 | 400 |
| Groove density (1/mm) | 1220 /366 | 1200 |
| Grating optimization | 1.5˚ / 4˚ | 150 nm |
| Grating coating | Au | Al+$MgF_2$ |
| Working range (eV) | 15-1800 | 2.5-20 |

**Table 6.** Technical parameters of microchannel plate photomultiplier used at BW3 beamline [66]

| Detector type | MCP-PMT 1645 U-09 Hamamatsu |
|---|---|
| Working range (nm) | 110-850 |
| Amplifier gain | $7x10^7$ (-3.0 kV) |
| Time resolution | 0.35ns |
| Dark pulses (1/s) | < 1 |
| Typical voltage (kV) | -3.0 |

The great advantage of storage rings with a large circumference, like DORIS was and PETRA presently in operation at DESY, is the possibility to perform time-resolved studies. Time-resolved excitation and emission were carried out at both beamlines used for experiments in Hamburg. The positrons were injected into the storage ring in bunches and the time interval between the bunches was either 192 ns or 96 ns in the case of 5 or 10 bunch filling, respectively. The typical width of the exciting pulse was 130 ps. Additional to time-integrated (TI) luminescence, spectra in two time windows with the length of $\Delta t$ and delay of $\delta t$ with respect to exciting synchrotron radiation pulse, were recorded (see Figure 3). FTW (fast time window) and STW (slow time window) are shown in Figure 3. Usually FTW had delay around $\delta t = 2$ ns and length around $\Delta t = 10$ ns and STW had delay around $\delta t = 100$ ns and length around $\Delta t = 50$ ns. Both setups allowed to record also luminescence decay curves in ns region using time-correlated photon counting technique.

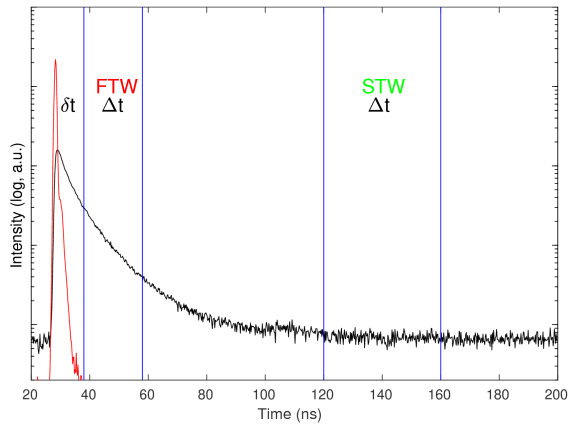


**Figure 3.** The measurement principle of the time-resolved luminescence detection technique using time windows. Black is decay curve for selected emission and red designates a real excitation pulse as recorded. Areas between blue lines mark FTW – fast time window or STW – slow time window.

# 5. SYNTHESIS OF ALUMINA NANOPOWDERS

Oxides can be synthesised in a many ways but broadly it is possible to divide methods into two broad categories “bottom-up” and “top-down” [67]. When a material is built up from atomic or molecular precursors which come together to form nanoparticles then this method is called “bottom-up”. The “bottom-up” method allows manipulating the properties (for example size, shape, stoichiometry, surface area etc.) of resulting nanoparticles [67]. “Top-down” is a method where you start from larger building blocks and physically tear down them to reach nanoscale [67]. Aluminium oxide can be synthesised in both ways. For example, “bottom-up” methods include sol-gel method [68], atomic layer deposition (ALD) method [20], physical and chemical vapour deposition [38] etc. An example of “top-down” method is electric explosion of aluminium wire [69]. In this work, the samples were prepared using plasma processing technique which is a top-down method [70] and by two “bottom-up” methods like combustion synthesis method [71] and oxidation of ultrapure aluminium [72]. In this work samples were synthesised by the author in Tartu as well as some of the samples were obtained from cooperation partners’ laboratories.

**Plasma processing technique and combustion synthesis method**

Two studied samples were prepared, using plasma processing technique [70] from raw alumina of 99.7% purity, in the Institute of Inorganic Chemistry (Riga, Latvia). Two different samples were produced for studies carried out with different crystallite size and named $Al_2O_3$ LV1 and $Al_2O_3$ LV2. The phase composition and crystallite size of these samples are given in Table 7.

Four studied samples were prepared using combustion synthesis method as described by Ianoş [71] in Tartu. In papers II and III the results obtained using combustion synthesis samples are presented. This method allows synthesising samples with different phase composition and crystallite size. For samples $Al_2O_3$ EE1, EE2, EE3 stoichiometric amounts of $Al(NO_3)_3{\cdot}9H_2O$ (Alfa Aesar, 99.999%) and urea (Alfa Aesar) as fuel were used with the fuel/nitrate molar ratio 5:2. The post-annealing process was applied to modify phase composition and crystallite size. Sample EE1, EE2 and EE3 were annealed in air at 1600 ºC for 5 hours, at 1100 ºC for 5 hours and at 1000 ºC for 1 hour, respectively. Sample EE4 was synthesised using a fuel-rich mixture with the fuel/nitrate molar ratio 25:4 and annealed in air at 1000 ºC for 1 hour. For sample EE4 the starting materials for synthesis were $Al(NO_3)_3{\cdot}9H_2O$ (REAHIM, 99.99%) and urea (Alfa Aesar).

Using a fuel-rich mixture, a lower combustion temperature is achieved and this results in different phase composition and higher specific surface area compared to the stoichiometric mixture [71]. The starting materials were dissolved in water and placed in a preheated oven at 500˚C. In the oven rapid exothermic combustion reaction takes place and white powder is produced as a product. As the alumina phase diagram is rather complex and the phase transition tempe-

ratures are not very well defined (e.g. depending also on precursor chemicals), therefore it is difficult to obtain pure transition alumina phases using this method. In this synthesis method usually α-$Al_2O_3$ and γ-$Al_2O_3$ are produced in different proportions [71, 73, 74]. The phase composition and crystallite size of these samples resulting from the combustion synthesis are given in Table 7.

**Oxidation of aluminium**

Three additional studied samples ($Al_2O_3$ FR1, $Al_2O_3$ FR2 and $Al_2O_3$ FR3) were prepared in Laboratory of Science of Processes and Materials (CNRS, France) using oxidation of high purity aluminium (99.999%) through a liquid mercury and silver film. This leads to the formation of macroscopic (cm size), but nano-structured (characteristic size of 10–200 nm) monoliths [72]. This method allows producing pure nano-sized $Al_2O_3$ and with different heat treatment, it is possible to affect the phase composition and crystallite size. The main impurities (Si, S, K, Na, Fe, P and Ca) are all together below $10^{-3}$ wt% and other minor impurities below $10^{-4}$ wt% [30]. The advantage of this method over combustion synthesis method is that the amount of impurities is well controlled as high purity aluminium is used in initial reaction phase. The phase composition and crystallite size of these samples are given in Table 7.

**Comparison of synthesis methods**

Synthesis methods using different raw materials can give different phase composition as shown in Figure 2. The phase transition temperatures are not well defined, so it is difficult to produce pure phase transition aluminas. At very high temperatures (>1100 ºC) the main phase will be α-$Al_2O_3$ with increasing crystallite size due to activation growth processes as a function of temperature.

Combustion synthesis method was selected due to its simplicity and efficiency in comparison with other methods. But it was obvious that one faces the problem of producing pure phase samples for transition aluminas and also it was difficult to tune the crystallite size with the post-annealing temperature selection. Plasma processing technique gives transition alumina phases but the samples contained more impurities than samples produced with other methods because this method is used for mass production of powders and the starting materials are usually less pure than for other synthesis routes. A problem with combustion synthesis is that it produces agglomerated particles. In comparison, the wire explosion method results in low aggregation products as shown by Kotov et al. [69].

In conclusion, as a result of using various synthesis methods, several samples of different phase compositions with different particle size distribution were available in this work.

# 6. CHARACTERISATION OF OBTAINED ALUMINAS

Crystallite size, morphology, particle size distribution, phase composition and specific surface area (SSA) of our studied samples were determined using different physical and chemical methods. There are different methods to analyse these characteristic properties. With X-ray diffraction analysis (XRD) it is possible to obtain information about the crystal structure, phase composition and average crystallite size. Surface and particle morphology can be studied with scanning electron microscopy (SEM) or transmission electron microscopy (TEM). SSA, which is the ratio of total surface area per unit of mass, can be measured using BET (Brunaur-Emmet-Teller) method. The phase composition and crystallite size information is collected in Table 7 for all studied samples.

**Alumina produced by plasma processing technique**

The characterisation of samples synthesised by plasma processing technique ($Al_2O_3$ LV1 and LV2) was done by collaborators in Latvia except for SEM measurements which were carried out in Tartu. According to XRD analysis, the phase composition of samples $Al_2O_3$ LV1 and LV2 were a mixture of θ- and δ-$Al_2O_3$ phases (Table 7). The average crystallite size was calculated from specific surface area measurements with spherical particle assumption. The particle size and morphology was checked by TEM, SEM and atomic force microscopy (AFM). The XRD patterns of these two samples and as a comparison gamma alumina XRD pattern are presented in Figure 4a. The main peaks overlap for γ-, θ- and δ-$Al_2O_3$ and without applying precise fitting procedures it is not possible to distinguish different alumina phases. The SEM pictures for samples $Al_2O_3$ LV1 and LV2 are presented in Figure 5a and 5b. There one can observe that the particle size is less than 100 nm and the particles are with spherical shape.

**Table 7.** Phase composition and crystallite size of alumina samples

| | Sample name | Phase composition | Average crystallite size |
|---|---|---|---|
| Plasma processing technique | $Al_2O_3$ LV1 | θ- and δ-$Al_2O_3$ | 75 nm<br>(SSA 25 $m^2$/g BET) |
| | $Al_2O_3$ LV2 | θ- and δ-$Al_2O_3$ | 40 nm<br>(SSA 50 $m^2$/g BET) |
| Combustion synthesis method | $Al_2O_3$ EE1 | α-$Al_2O_3$ | 180 nm (XRD) |
| | $Al_2O_3$ EE2 | α-$Al_2O_3$ (~30–40%)<br>γ-, θ- and δ-$Al_2O_3$ | 100 nm (XRD) |
| | $Al_2O_3$ EE3 | α-$Al_2O_3$ (~15–20%)<br>γ-$Al_2O_3$ (~80–85%) | 100 nm (XRD)<br><10 nm (XRD) |
| | $Al_2O_3$ EE4 | α-$Al_2O_3$ (~40–50%)<br>γ-$Al_2O_3$ (~50–60%) | 80 nm (XRD)<br><10 nm (XRD) |

| | Sample name | Phase composition | Average crystallite size |
|---|---|---|---|
| Oxidation of aluminium | $Al_2O_3$ FR1 | α-$Al_2O_3$ | 200–300 nm (SSA 5–10 $m^2$/g BET) |
| | $Al_2O_3$ FR2 | θ-$Al_2O_3$ with traces of α-$Al_2O_3$ | 10 nm (SSA 110 $m^2$/g BET) |
| | $Al_2O_3$ FR3 | γ-$Al_2O_3$ | 7 nm (SSA 150 $m^2$/g BET) |

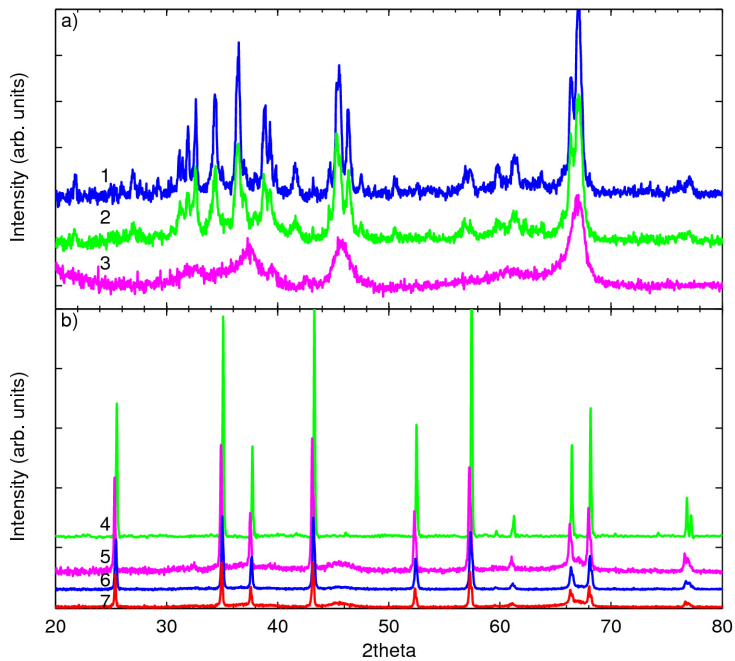


**Figure 4.** XRD patterns for studied alumina samples a) blue (1) – $Al_2O_3$ LV1, green (2) – $Al_2O_3$ LV2 magenta (3) – Alfa Aesar $Al_2O_3$ gamma, b) green (4) – $Al_2O_3$ EE1, magenta (5) – $Al_2O_3$ EE2, blue (6) – $Al_2O_3$ EE4, red (7) – $Al_2O_3$ EE3.

**Alumina produced by combustion synthesis**

The characterisation of samples $Al_2O_3$ EE1, EE2, EE3 and EE4 were performed in Tartu by the author. For samples $Al_2O_3$ EE1, EE2, EE3 and EE4, which were prepared by combustion synthesis, crystallite size and phase composition were determined by XRD analysis. The XRD patterns for these samples are presented in Figure 4b. From XRD analysis using the Rietveld method, it was possible to calculate quantitative phase composition. The problem, in this case, is the partial overlap of XRD patterns of different alumina metastable phases and broad lines of γ-$Al_2O_3$ which are seen in Figure 4b. Due to this the phase compositions are deduced approximately. Sample $Al_2O_3$ EE1 was a pure

α-phase sample as it was purposely post-treated at 1600°C for 5 hours, which is far above α-$Al_2O_3$ formation temperature. Such treatment resulted in the largest crystallite size of 180 nm, but still in nanoscale. Samples $Al_2O_3$ EE2, EE3 and EE4 were composed of mixed alumina phases. The main phases observed for these samples were α- and γ-phases in different proportions as shown in Table 7. For sample $Al_2O_3$ EE2, which was treated at 1100°C for 5 hours, high-resolution luminescence studies in the visible range, which are by far more sensitive than XRD, showed that there were luminescence peaks, which correspond to θ-$Al_2O_3$ phase. Other unidentified phases can be present in this sample as well. It is not possible to say what is the exact phase composition for this sample but dominating phases are α- and γ-$Al_2O_3$. Crystallite size was estimated using the Scherrer equation for samples prepared by the author and the respective values are given in Table 7. γ-$Al_2O_3$ has a few very broad peaks in XRD pattern and because of that it is difficult to estimate the exact crystallite size for this phase but the calculations showed that it is below 10 nm for samples $Al_2O_3$ EE2, EE3 and EE4. The crystallite size of α-$Al_2O_3$ phase was for sample $Al_2O_3$ EE1 180 nm, for samples $Al_2O_3$ EE2 and EE3 100 nm, and for sample $Al_2O_3$ EE4 80 nm. The size of α-$Al_2O_3$ crystallites in the sample depends on synthesis conditions and post-annealing temperatures and length. The crystallite size is smaller for EE4 than for EE3 although the same post-treatment procedure, 1 hour at 1000°C, was used for both samples. But for the $Al_2O_3$ EE4 fuel rich synthesis route was applied while for the EE3 sample stoichiometric amounts of starting materials were used. Since the resulting crystallite size is larger for the EE3, which indicates that higher temperatures were in the reaction zone. On the other hand, for phase composition, the effect is opposite as in the EE4 sample the amount of α-$Al_2O_3$ is larger than in the EE3 and even in the EE2 sample, which would be proof of the opposite taking only temperature into account. It is obvious that influence of various reaction parameters of combustion synthesis is more complicated than simple analysis can provide. Morphology of nanoparticles was checked using SEM method. The SEM images are presented in Figure 5, which show that the crystallites are agglomerated into larger particles with a size of few hundred nanometres up to a couple of micrometres.

**Alumina produced by oxidation of aluminium**

Crystallite size and phase composition of the samples $Al_2O_3$ FR1, FR2 and FR3 were studied by collaborators in France. The crystallite size for these samples are 200–300 nm for $Al_2O_3$ FR1, 10 nm for $Al_2O_3$ FR2 and 7 nm for $Al_2O_3$ FR3 [30]. These samples had pure phase composition according to the producers. The SEM images (Figure 6) of these samples show that morphology of the samples is different from other samples as the samples consist of ultraporous monoliths, which are composed of tangled alumina fibres. On TEM images (Figure 6) one can resolve more detailed the morphology of the nanoparticles formed in the applied aluminium oxidation process. For samples $Al_2O_3$ FR1 the particles are around 200 nm with small rod shape. Samples $Al_2O_3$ FR2 and $Al_2O_3$ FR3 have tangled fibrous structures (see Figure 6).

## Conclusion

Morphology of these three classes of samples is quite different. In samples LV1 and LV2 we can see small particles which are not agglomerated to larger ones (Figure 5a and 5b). On the contrary, in combustion synthesised samples $Al_2O_3$ particles are agglomerated into larger units (Figure 5c-5f). The smaller alumina particles of samples $Al_2O_3$ FR1, FR2 and FR3 are agglomerated forming fibre-like structures (Figure 6). This shows that powders manufactured in three different methods give completely different morphology of the particles which can influence the outcome of luminescence studies (see Section 7). The average crystallite size is different for different alumina phases. Due to differences in the phase transformation temperatures, the $\alpha$-$Al_2O_3$ has the largest crystallite size and $\gamma$-$Al_2O_3$ the smallest one with the other phases in between these two.

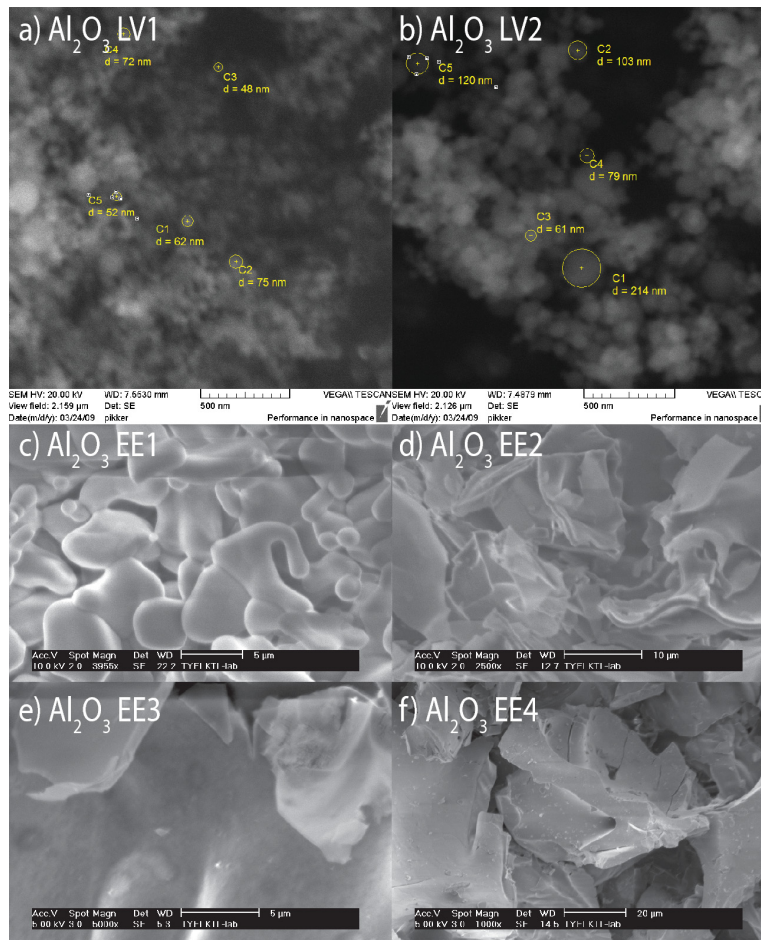


**Figure 5.** SEM pictures of studied alumina samples using plasma processing method (a, b) in Latvia and combustion synthesis method (c, d, e, f) in Tartu.

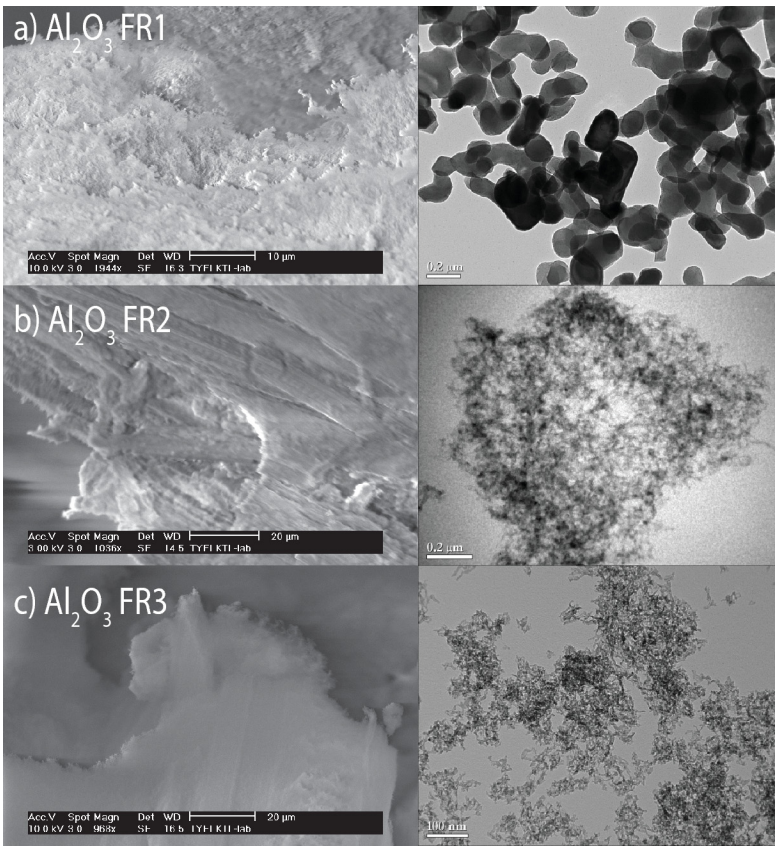


**Figure 6.** SEM (on left) and TEM (on right) pictures of samples produced using oxidation of aluminium method in France.

# 7. LUMINESCENCE STUDIES OF MIXED TRANSITION ALUMINA

## 7.1 Intrinsic absorption onset of different alumina nanopowders

In order to determine the onset of intrinsic absorption, we studied the excitation spectra for centres, which are intrinsic by their nature. Usually, absorption and reflection spectroscopy is applied in such studies, but the alumina samples are powders, which are neither transparent nor reflective, thus does not enable such measurements.

In paper III the shift of exciton excitation band was revealed and discussed. Figure 7 shows excitation near the intrinsic absorption region at 10 K for 7.6 eV STE emission for samples $Al_2O_3$ EE1, $Al_2O_3$ FR1 and $Al_2O_3$ single crystal. These three samples consisted only of α-$Al_2O_3$ phase. One can observe a 0.15 eV shift in the onset of intrinsic absorption towards higher energies in nanopowders compared to the single crystal. This effect can be caused by the anisotropy of material, the size of crystallite or stress effects as discussed below (Paper III).

Firstly, $Al_2O_3$ is an anisotropic material (see [23]) and small shifts can occur due to sample's different orientation with respect to the polarized synchrotron radiation. This effect has been shown in low-symmetry materials, for example in tungstate crystals [75]. However, the studied single $Al_2O_3$ crystal had the c-axis in the direction normal to the incident synchrotron radiation and there should be no orientation effects (paper III). One can assume that crystallites in nanopowders are randomly oriented with respect to the polarised synchrotron radiation, therefore no orientation effects can be expected.

Secondly, the studied alumina powder samples had crystallites sizes around 200 nm, therefore the possibility of quantum confinement effects is negligible. The nano-size of crystallites can cause these effects for excitons with dimensions comparable to crystallites. Confinement effects of large radius excitons have been investigated in multiple works (see e.g. [75]). But there is a significant difference in the case of alumina, where only strongly localised intrinsic excitations, so called self-shrunk excitons, have been observed [23]. These excitons have a radius comparable to a lattice constant and their electronic states cannot be influenced by crystallite size of 200 nm. In $CdWO_4$ thin films, the shift of the intrinsic absorption onset to higher energies by 0.4 eV compared to single crystals has been found and it was explained through differences in optical density of thin films and thick crystal sample [76]. It is not the case for alumina nanopowders as the studied samples were macroscopically thick like crystals.

Thirdly, there have been considerations of residual stress effects due to the treatment of sample surface, which can cause shifts of spectral features in the reflection spectra [77]. In our case, no special treatment of powders was done,

but in our opinion (see paper III) the observed shift can still be induced by residual stresses produced during synthesis process of aluminas.

Generally, (nano)powder samples are known to behave differently than single crystals with a displacement of excitation features. The studies performed revealed such shift in nanopowder samples, but also in alumina ceramics [78] with micrometre size crystallites with sample morphology more like that of macroscopic crystals. Therefore, there is a good ground to assume that further studies are needed to provide a detailed explanation.

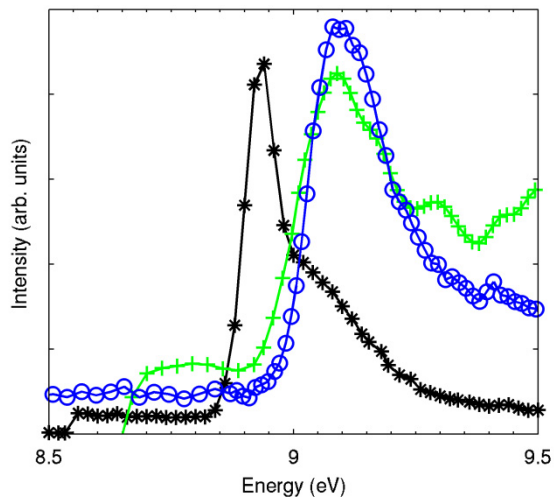


**Figure 7.** TI excitation spectra for 7.6 eV luminescence at 10K. Black (*) – $Al_2O_3$ crystal; Green (+) – $Al_2O_3$ EE1 and blue (O) – $Al_2O_3$ FR1.

**Intrinsic absorption of θ-$Al_2O_3$**

For samples $Al_2O_3$ LV1 and LV2 the intrinsic absorption onset at 7.5 eV was determined in paper I. This result is illustrated by excitation spectra for the UV emissions in samples $Al_2O_3$ LV1 and LV2, which are presented in Figure 8 a2. Taking into account that these samples are the mixture of δ- and θ-$Al_2O_3$, it is not possible to determine the onset of fundamental absorption for these phases separately. On the other hand, the bandgap value of 7.6 eV for pure θ-$Al_2O_3$ has been reported by Museur et al. [30]. For reference, the spectrum of $Al_2O_3$ FR2, which is mostly pure θ-$Al_2O_3$ synthesised by Museur team, but measured by our group is also presented in Figure 8 a2. As a result, it is clearly observable from Figure 8 a2 that the excitation onset for all samples is at the same energy at 7.5 eV. In the transparency range, there is a low energy excitation peak at 5.4 eV in the FR2 nanopowders, which is due to defect states (see section 7.4). For δ-$Al_2O_3$ the onset of intrinsic absorption was reported at 7.2 eV [31] and it was ascribed to the intrinsic absorption of $AlO_4$ cells. It is likely that in the LV1

and LV2 nanopowders the contribution of δ-$Al_2O_3$ is lower because the δ-phase formation temperature range (900–1000 °C) is below of that for θ-phase [4]. Therefore, there are no clear indications of δ-phase in the excitation spectra.

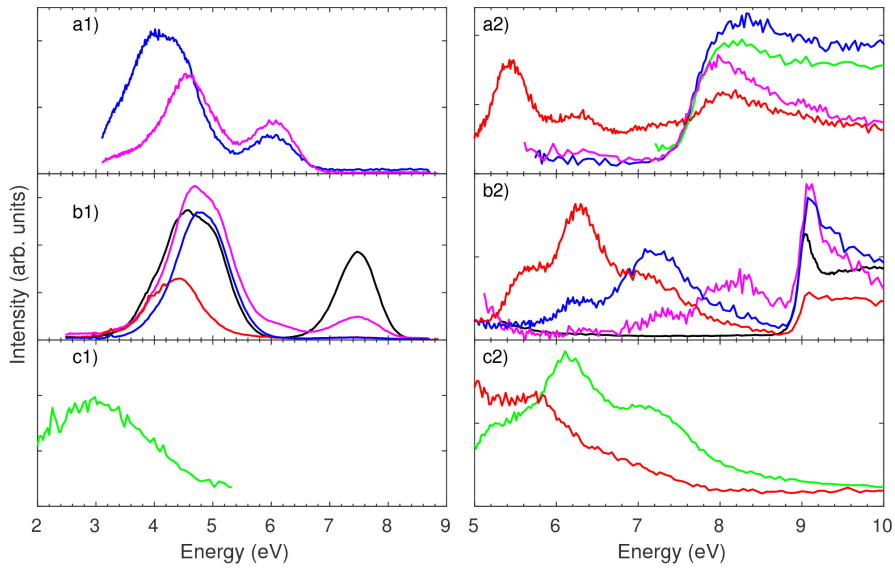


**Figure 8.** Emission spectra (a1, b1) excited with 130 eV photons and (c1) with 9.5 eV photons on the left at 8K. Excitation spectra for the emissions in the UV region of alumina nanopowders on the right at 8K. a1) blue – $Al_2O_3$ LV1 and magenta – $Al_2O_3$ LV2 a2) blue – $Al_2O_3$ LV1 excitation for 4.4 eV, green – $Al_2O_3$ LV1 excitation for 5.5 eV, magenta – $Al_2O_3$ LV2 excitation for 4.4 eV, red – $Al_2O_3$ FR2 (θ-$Al_2O_3$) excitation for 4.1 eV. b1) black – $Al_2O_3$ EE1, magenta – $Al_2O_3$ EE2, red – $Al_2O_3$ EE3 and blue $Al_2O_3$ EE4. b2) black – $Al_2O_3$ EE1 excitation for 4.6 eV, magenta – $Al_2O_3$ EE2 excitation for 4.5 eV, red – $Al_2O_3$ EE3 excitation for 4.1 eV and blue $Al_2O_3$ EE4 excitation for 4.3 eV. c1) green – emission for 9.5 eV excitation of γ-$Al_2O_3$ nanopowders. c2) red – diffuse reflectivity and green – excitation for 3.1 eV emission of γ-$Al_2O_3$ nanopowders.

### Intrinsic absorption of γ-$Al_2O_3$

In the paper II, the intrinsic absorption onset of 7.0 eV for γ-$Al_2O_3$ was discussed using the recorded γ-$Al_2O_3$ diffuse reflection spectrum and the excitation spectra for $Al_2O_3$ EE2 – EE4 nanopowders composed of mixed alumina phases. Diffuse reflection spectrum provides data on host absorption for non-transparent powder samples. Especially useful in cases when supported by luminescence excitation spectra. For γ-$Al_2O_3$ powder diffuse reflection spectrum shown in Figure 8 c2, a decreasing of intensity occurs in the range of 6.2–8 eV followed by a constant plateau above 8 eV. This points to the beginning of the host absorption being below 7.0 eV. The excitation spectrum

for 3.1 eV emission has a band peaking at 6.2 eV, which is followed by a broader band covering energy range of 6.8–7.8 eV.

In Figure 8 b2, the excitation spectra for $Al_2O_3$ EE1 – EE4 nanopowders are shown. For the sample EE2, which was a mixture of different phases (mostly γ, θ, α), one can distinguish several onsets in excitation spectrum when energy increases (Figure 8 c2). The first step is at 6.8–7 eV, which is correlated with the broad excitation band at 7.0 eV in Figure 8c. It is attributed to the onset of γ-$Al_2O_3$ host absorption. The second step occurs at 7.5 eV, which was attributed before to the θ-$Al_2O_3$ host absorption and the third step at 9 eV corresponds to the onset of intrinsic absorption of α-$Al_2O_3$ (Paper II and references therein). These two results are congruent and allow to assign the energy region above 7 eV to host absorption of γ-$Al_2O_3$ (Paper II). Later, the start of intrinsic absorption of 6.85 eV for γ-$Al_2O_3$ was reported by Museur et al. [30], which coincides well with our measurements.

These experimental results can be compared with the values from theoretical studies carried out by different authors (see Section 3). According to the studies the band gap value decreases in the following order $\alpha > \kappa > \theta > \gamma$, with values of 6.72 eV, 5.49 eV, 5.04 eV, 4.40 eV [15]. It occurs due to the lowering of conduction band states by the introduction of $AlO_4$ structural units. Although these theoretical values are underestimated due to a known shortage of DFT calculations, the trend and differences in band gap values are in good agreement with the experimental values for different alumina phases.

In conclusion, we investigated the electronic structure of aluminas including the onset of intrinsic absorption for the mixture of δ- and θ-$Al_2O_3$ and as well as for γ-$Al_2O_3$ and α-$Al_2O_3$ nanopowders. To the best of our knowledge, this was the first report on the γ-$Al_2O_3$ band gap value deduced by luminescence methods. A shift of the onset of intrinsic absorption for nanopowders in comparison with a single crystal of α-$Al_2O_3$ was revealed being attributed to residual stresses introduced during synthesis of nanocrystals.

## 7.2 Intrinsic luminescence in the UV and VUV range

In Figure 9 (left panel) the emission spectra under 130 eV photons and 5 keV electron-beam excitation at 8 K for combustion and plasma processing synthesised nanopowders are visualised. In Figure 10 similar spectra for nanopowders produced in France (FR1, FR2 and FR3) are depicted as well. The origin of luminescence bands was discussed in papers I, II and III for different samples. As discussed in Section 3 the main defects in alumina are F- and $F^+$-centres with emissions peaking at 3.0 and 3.8 eV, respectively. In our samples (Figure 9) luminescence in two regions covering VUV and UV-visible region were investigated. For combustion synthesis $Al_2O_3$ EE1 – EE4 nanopowders (Figure 9 a1 – d1) and for samples FR1 and FR2 (Figure 10 a1 and b1), the VUV band peaking at 7.6 eV and the UV band with a maximum at 4.5 eV were detected. Samples $Al_2O_3$ LV1 and LV2 have two emission bands with maxima

at 4 and 6 eV (Figure 9 e1 and f1). Sample FR3 had broad band covering region from 2 – 5 eV (Figure 10 c1).

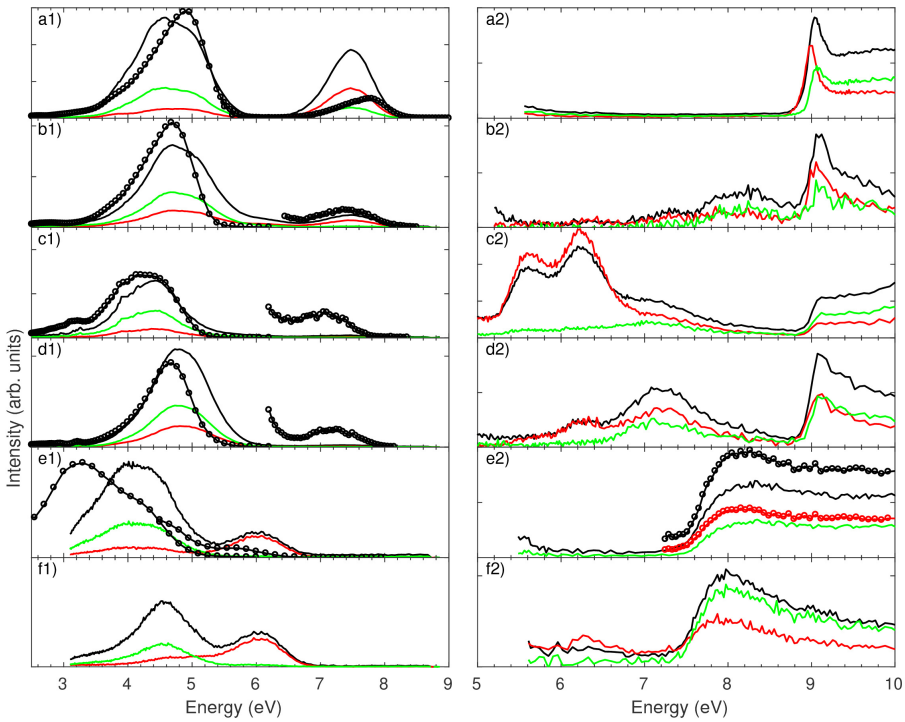


**Figure 9.** Emission spectra excited by 130 eV photons at BW3 and with electrons on the left and excitation measured at SUPERLUMI setup on the right at 5 – 8 K. Black lines indicate time integrated (TI) spectra, red lines correspond to luminescence recorded in fast time window (FTW), green lines correspond to slow time window (STW). Black circles on the left indicate TI cathodoluminescence spectra measured at 8 K with 5 keV electrons. Time window values were for FTW $\delta t \approx 2$ ns and $\Delta t \approx 10$ ns and for STW $\delta t \approx 100$ ns and $\Delta t \approx 50$ ns. a1) $Al_2O_3$ EE1 PL and CL emission spectra; a2) Excitation spectrum for 4.6 eV emission; b1) $Al_2O_3$ EE2 PL and CL emission spectra; b2) Excitation spectrum for 4.5 eV emission; c1) $Al_2O_3$ EE3 PL and CL emission spectra; c2) Excitation spectrum for 4.1 eV emission; d1) $Al_2O_3$ EE4 PL and CL emission spectra; d2) Excitation spectrum for 4.1 eV emission; e1) $Al_2O_3$ LV1 PL and CL emission spectra; e2) Excitation spectrum for 4.5 eV emission (lines), excitation spectrum for 5.5 eV emission (circles); f1) $Al_2O_3$ LV2 PL emission spectrum; f2) Excitation spectrum for 4.4 eV emission.

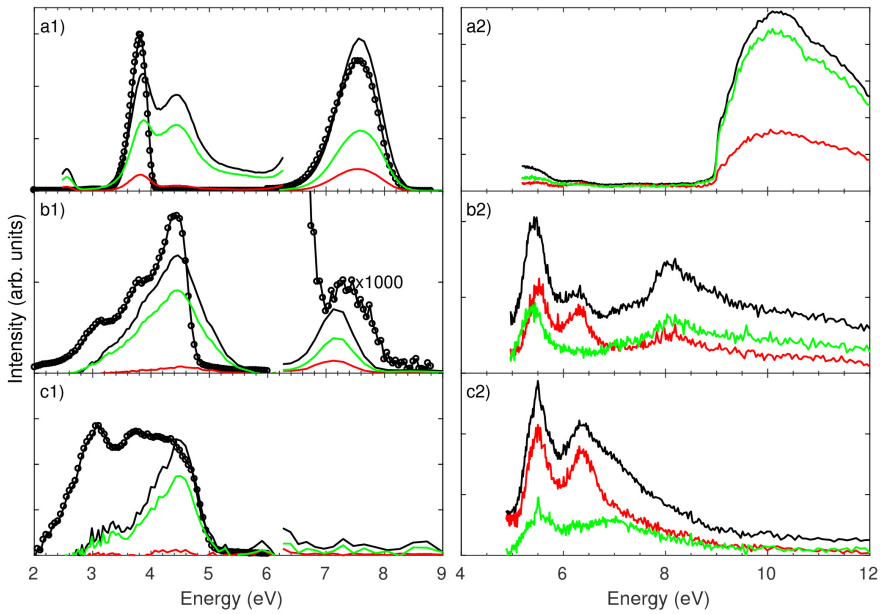


**Figure 10.** Emission spectra excited by 130 eV photons at BW3 and with 10 keV electrons on the left and excitation measured at SUPERLUMI setup on the right at 8 K for samples FR1-FR3. Black lines indicate time integrated (TI) spectra, red lines correspond to luminescence measured in fast time window (FTW), green lines correspond to slow time window (STW). Black circles on the left designate TI cathodoluminescence spectra measured at 8 K with 10 keV electrons. Time window values for spectra measured at BW3 were for FTW $\delta t \approx 1$ ns and $\Delta t \approx 5$ ns and for STW $\delta t \approx 15$ ns and $\Delta t \approx 65$ ns. Time window values for spectra measured at SUPERLUMI were for FTW $\delta t \approx 2$ ns and $\Delta t \approx 10$ ns and for STW $\delta t \approx 100$ ns and $\Delta t \approx 50$ ns. a1) $Al_2O_3$ FR1 PL and CL emission spectra; a2) Excitation spectrum for 4.2 eV emission. b1) $Al_2O_3$ FR2 PL and CL emission spectra; b2) Excitation spectrum for 4.1 eV emission. c1) $Al_2O_3$ FR3 PL and CL emission spectra; c2) Excitation spectrum for 4 eV emission.

**STE emission at 7.6 eV and 6 eV**

The highest intensity of 7.6 eV luminescence among studied samples was detected for the samples $Al_2O_3$ EE1 and FR1 (Figures 9 a1 and 10 a1), which arises from a combination of pure α-$Al_2O_3$ phase composition and the largest crystallite size (180 nm and 200–300 nm, respectively). The decrease of crystallite size and amount of α-phase results in the increasing probability of non-radiative transitions at crystallite facets, leading to lower intensities for 7.6 eV emission in other nanopowders. The VUV band is shifting also towards lower energies when the amount of α-$Al_2O_3$ decreases (Figure 9 a1 – d1) in samples $Al_2O_3$ EE1 – EE4. This effect can be accounted to reabsorption of VUV luminescence by transition aluminas (especially γ-$Al_2O_3$), which have the onset of intrinsic absorption at 7 eV (Section 7.1 and paper II). Also, changes in

phase composition of nanopowders in favour of a bigger share of transition aluminas leads to the corresponding decrease of the intensity of 7.6 eV emission. In $Al_2O_3$ FR2 nanopowder the 7.6 eV band is detectable although shifted to lower energies. According to the XRD analysis the sample should have only pure θ-$Al_2O_3$ phase. As the 7.6 eV emission is characteristic to α-$Al_2O_3$ then it is possible to conclude that in this sample certainly small amount of α-$Al_2O_3$ phase is present, which is a demonstration of the possibility to distinguish different alumina phases using luminescence spectroscopy.

As was mentioned in the description of used experimental setups (section 4) the time-resolved measurements provide very valuable characterization parameters for dynamics of electronic excitations in the studied nanopowders. In the analysis of the decay kinetics, the excitation regime (the value of excitation energy) must be taken into consideration (see the overview of earlier time-resolved studies on 7.6 eV emission in section 3). We recorded decay kinetics for 7.6 eV emission under 130 eV photon excitation of BW3 synchrotron beamline at DESY in Hamburg. As was expected for the case of inner shell excitation, the obtained decay curves were non-exponential. Applied numerical fit resulted in a sum of three exponents, which gave the following values of time constants: 0.4, 2.4 and 18.4 ns; 0.4, 1.6 and 5.6 ns; 0.1, 0.4 and 7 ns; 0.2, 0.9 and 5 ns for $Al_2O_3$ EE1, EE2, EE3 and EE4, respectively. The fastest components of numerical fit results are comparable with the detector response time and therefore should be considered as a detection limit without further interpretation. These results indicate that the luminescence decay processes in nanopowders are faster than in single crystals [29]. This effect can be explained by non-radiative relaxation channels, which are becoming more dominant with decreasing of crystallite size (Paper II). For sample $Al_2O_3$ EE1 we were able to register the decay of 7.6 eV emission also under direct exciton excitation using 9 eV photons at SUPERLUMI setup. The measured decay time for this case was 2.7 ns, which is considerably shorter than found for the α-$Al_2O_3$ crystal with a typical single exponential decay time of 7 ns [29]. This shortening is also assigned to a smaller crystallite size, which increases the probability of non-radiative decay channels.

In samples $Al_2O_3$ LV1 and LV2 no luminescence at 7.6 eV was revealed, but instead of this the fast luminescence at 6 eV was found (Figure 9 e1 and f1). The decay of this band can be approximated by the sum of two exponents with time constants of 0.5 ns and 3.9 ns for sample LV1 (excited at 130 eV) and 0.93 ns and 8.4 ns for sample LV2 (excited at 100 eV), respectively. Photo-excitation at lower energies (10.8 eV) performed at the SUPERLUMI station resulted in decay time components of 2.2 and 13.3 ns. Its fast decay (comparable to 7.6 eV STE emission of α-$Al_2O_3$ phase in other samples) and excitation spectrum for this emission (see Figure 9 e2), which has the onset at ~7.5 eV with the fast component dominating, strongly support our interpretation for this 6 eV emission as singlet STE emission in θ-$Al_2O_3$ phase (Paper I) which was confirmed by results of later study reported by Museur et al. [30].

Regarding the origin of VUV bands at 7.6 and 6 eV, it can be concluded that both are due to radiative decay of singlet type STE with a lifetime in ns range of different phases. The α-$Al_2O_3$ consists of $AlO_6$ structural units, whereas θ-$Al_2O_3$ is built up of both $AlO_6$/$AlO_4$ units in 1:1 ratio. The different local geometry of latter ones is probably responsible for different STE properties in θ-$Al_2O_3$ phase. The decay time of STE emission in nanopowders is affected by the influence of crystallite size mainly due to non-radiative relaxation channels, which are becoming more dominant with decreasing of crystallite size and results in shortened lifetime of electronic states.

**STE emission at 4.6 eV**

Strong luminescence was discovered in the UV range of 4–5 eV (Figure 9 a1 to f1 and 10 a1 to c1) in all studied alumina nanopowders with varying peak positions. This 4.6 eV emission has dominating slow decay (750–780 μs component), as revealed in pulsed cathodoluminescence study (see Figure 11). This observation and faster ns components observed under XUV excitations (Figure 9, left panel, spectra in fast and slow time window designated by red and green lines, respectively) suggest that there are several overlapping luminescence centres present in nanopowders. The phenomena related to the defects will be discussed later in section 7.3. Both XUV and steady electron beam excitation resulted in rather similar emission spectra. The excitation spectra for these UV emissions in the Figure 9 a2 to f2 and Figure 10 a2 to c2 depend on particular phase compositions of samples. The absence of excitation bands in the transparency range (Figure 9 a2, b2, e2, f2 and Figure 10 a2) points to its intrinsic nature. The 750–780 μs lifetime of 4.6 eV emission supports the assumption that it is due to radiative decay of triplet STE (see our Papers I, II and III, and results in [30]).

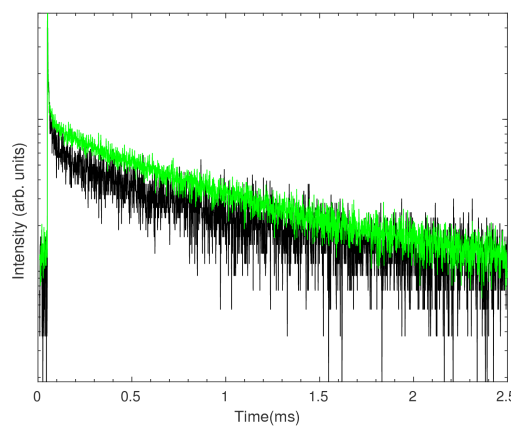


**Figure 11.** Decays for 4.6 eV emission under pulsed electron excitation at T = 78 K. Decays were fitted with one exponential and values are given in the brackets. Black – $Al_2O_3$ EE1 (τ = 750 μs); green – $Al_2O_3$ EE4 (τ = 780 μs).

## 7.3 Defect luminescence in aluminas

In alumina, there are a plenty of different defect centres, which influence material performance, participate in relaxation processes of electronic excitations and can be investigated using luminescence as was discussed in section 3. The most well-known are F- and $F^+$-centres having luminescence at 3.0 and 3.8 eV, respectively in alumina crystals (see section 3 for details). For transition, aluminas there is some information about how the properties of these main centres change and which type of centres are present in transition aluminas (see section 3 for details). In this section, the defect luminescence in transition and nano-size aluminas will be discussed.

**Defect centre luminescence in nano-size α-$Al_2O_3$**

In Figure 12 emission and excitation spectra for two nanopowders, $Al_2O_3$ EE1 and FR1, containing only α-$Al_2O_3$ are presented. Crystallite sizes of these samples are 180 nm and 200–300 nm for $Al_2O_3$ EE1 and FR1, respectively. Studies revealed that the behaviour of luminescence is different for these samples. Sample EE1 possesses slow luminescence component peaked at 3.0 eV (Figure 12 a1) with the dominating excitation band at 6.0 eV (Figure 12 a2), which correspond very well to the F-centre luminescence properties in the α-$Al_2O_3$ crystal ([19] and Section 3). Using pulsed electron beam excitation, the measured decay was 23 μs (Paper III), which is significantly shorter compared to 36 ms revealed for F-centre in single crystals earlier (Section 3) However, the pulsed CL experimental conditions are not suited for exploring ms time range. Kortov et al. reported for 3 eV emission decay times under electron excitation below 1 μs in nanoceramic alumina samples [79].

Looking at sample FR1 the fast luminescence dominates, peaking at 3.1 eV (Figure 12 b1) and this emission has rather complicated excitation spectrum with the bands at 5.2, 6.0 and 7.3 eV (Figure 12 b2). The decay times of this luminescence remain unchanged and were equal to 1.5 and 8 ns when excited with 5.2 eV or 6.2 eV photons. This complicated excitation band structure and fast decay times are similar to $F^+$-centre excitation spectrum where excitation bands were found at 4.8, 5.4 and 6 eV with a decay time of 2 ns in α-$Al_2O_3$ single crystals (see section 3). This luminescence centre can be due to either a surface defect or regular $F^+$ centre with a large red shift of its emission in comparison to single crystals. Under electron beam excitation and by XUV photons for the nano-size sample FR1 the well pronounced 3.8 eV band with decay components of 1.9 and 26 ns was revealed (Figure 10 a1). Under pulsed electron beam excitation for the decay of 3.8 eV luminescence band, the longer luminescence components 0.7 and 29 μs were also identified (Paper III), indicating that complicated relaxation processes take place together with overlapping luminescence centres of different nature. According to Surdo et al. [24], an additional slower decay component appears for $F^+$-centre's luminescence when the excitation energy increases. As cathodoluminescence and XUV excitation are less surface sensitive compared VUV excitation one can observe

differences in the recorded emission spectra (see Section 4 for details). Taking into account all experimental results, which do not support the remarkable red shift of $F^+$ luminescence centre by 0.7 eV, there has to be another explanation.

Hence the 3.1 eV emission band is more likely linked to surface effects as the powder has nano-size crystallites (200–300 nm) and the emission band is relatively stronger when surface sensitive experimental conditions were applied. Therefore this 3.1 eV band is assigned to the surface $F^+$-centres ($F^+_s$), which has been previously described and discussed by Gorbunov et al. [42]. In the present case, the excitation bands positions are in agreement with ones at 5.24, 6.13 and 7.44 eV with a decay of 0.5 and 5 ns recorded by Gorbunov et al. [42]. In the present study, fast decay components are slower (1.5 and 8 ns) in the sample EE1 than that of Ref 42. Although studied nanopowders have even smaller crystallite size, the agglomeration of nanoparticles can influence dynamics, as was discussed in Section 6. Therefore, the fastest component below 1 ns is not observed in the present case. One cannot exclude the influence of various synthesis methods used as these can produce nanocrystallites with different defect composition. Although the fast luminescence component is dominating in the sample FR1, there are slow components present, with decay components 0.4 and 5 μs (Paper III). Obviously, F-centre contributes to revealed emission, although the typical excitation band at 6 eV for slow luminescence is absent, which usually points to the presence of F-centres (see Figure 12 b2).

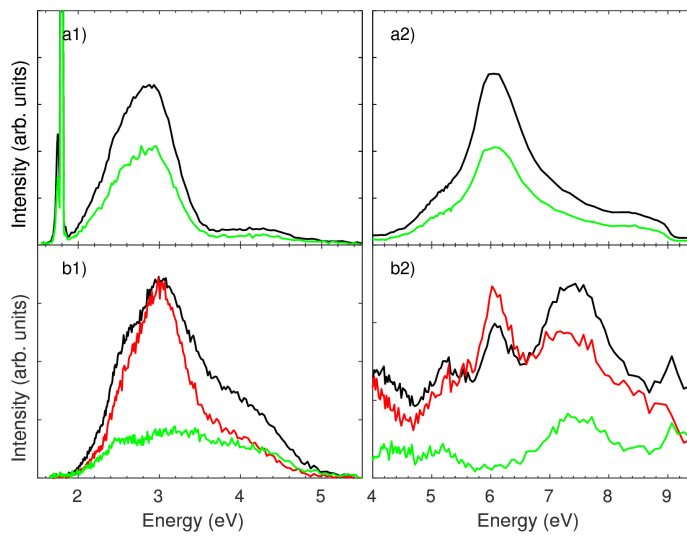


**Figure 12**. Emission and excitation spectra for pure α-$Al_2O_3$ nanopowders at 8 K. Time-integrated (TI) – black, FTW – red and STW – green line. Time window values were for FTW $\delta t \approx 2$ ns and $\Delta t \approx 10$ ns and for STW $\delta t \approx 100$ ns and $\Delta t \approx 50$ ns. a1) $Al_2O_3$ EE1 – emission spectrum excited by 7.1 eV photons; a2) excitation spectrum for 2.88 eV emission; b1) ultra-porous $Al_2O_3$ FR1 (α-$Al_2O_3$) – emission spectrum excited by 7.0 eV; b2) excitation spectrum for 3.1 eV emission.

**Defect centre luminescence in nanopowders composed mainly of θ-$Al_2O_3$**

Results of luminescence study for primarily θ-$Al_2O_3$ containing samples LV1 and FR2 are depicted in Figure 13. There is a similar fast luminescence component at 3 eV as shown for the sample FR1. This 3 eV luminescence in the sample LV1 has excitation bands at 5.1, 5.8 and 7.1 eV (Figure 13 a2 circles) and the decay components of this luminescence were 3.6 and 11.6 ns when excited with 7.1 eV photons. These values are similar to the ones obtained for FR1. In the case of FR2 nanopowder, there is the strongest feature a broad excitation band at 6 eV and we do not see other bands at the side (Figure 13 b2 lines). The 6 eV excitation band contains both slow and fast emissions, so the presence of two different centre emissions cannot be excluded. The decay time of this centre emitting at 3.1 eV has two components 1.7 and 8.6 ns using 6 eV photon excitation. These values are similar to those observed for the FR1 sample and therefore a similar explanation is given proposing the existence of surface $F^+$-centres also in these samples although there are some differences in the excitation spectra.

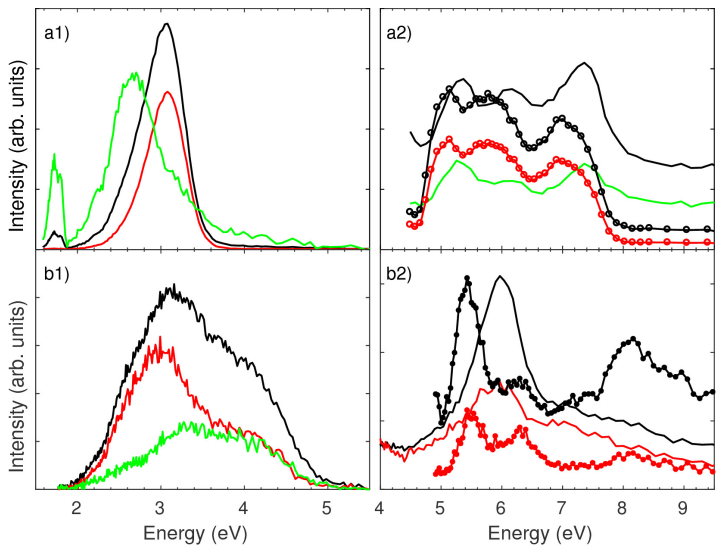


**Figure 13.** Emission and excitation spectra for nanopowders composed mainly of θ-$Al_2O_3$ at 8 K. Time window values were for FTW $\delta t \approx 2$ ns and $\Delta t \approx 10$ ns and for STW $\delta t \approx 100$ ns and $\Delta t \approx 50$ ns. Time-integrated (TI) – black, FTW – red and STW – green line or symbols. a1) $Al_2O_3$ LV1 – emission spectrum excited with 7.1 eV photons; a2) excitation spectrum for 2.5 eV emission (lines) and excitation spectrum for 3.1 eV emission (circles); a1) ultra-porous $Al_2O_3$ FR2 (θ-$Al_2O_3$) – emission spectrum excited with 7.0 eV photons; b2) excitation spectrum for 3.1 eV (lines) and 4.1 eV (circles) emission.

For the LV1 nanopowder, there is also a slow emission peaked at 2.6 eV with rather complicated excitation band structure. The excitation bands have maxima at 5.4, 6.2 and 7.4 eV. This red shifted band is interpreted this as F-centre luminescence (Paper I). But performed experiments did not confirm the existence of similar slow luminescence band in the sample FR2.

Additional fast luminescence is observed in the sample FR2 present as a shoulder at 4.1 eV. Although in $\alpha$-$Al_2O_3$ luminescence in UV peaked at 4.6 eV was attributed to self-trapped exciton luminescence (see Section 7.3), in this sample the excitation spectrum recorded at 4.1 eV contains multiple excitation bands in the transparency range excluding its intrinsic nature (see Figure 13 b2). The bands are located at 5.4 and 6.3 eV and the luminescence is also excited through the energy transfer processes in the intrinsic absorption region for $\theta$-$Al_2O_3$ (>7.5 eV, see section 7.1). The decay time of this centre has two components 1.2 and 9.7 ns, and 2.4 and 20.5 ns when excited with 5.5 and 8 eV photons, respectively. Due to its fast nature and spectral location in the region typical for $F^+$-centre, it is attributed to the $F^+$-centre luminescence.

**Defect centre luminescence in nanopowders composed mainly of $\gamma$-$Al_2O_3$**

Sample $Al_2O_3$ EE3 was mainly composed of $\gamma$-$Al_2O_3$ (see Table 7) and the sample FR3 consist of pure $\gamma$-$Al_2O_3$. However, rather similar luminescence spectra were observed for both these samples like in other transition aluminas. The main luminescence band covers region from 2 to 5 eV with bands peaked near 3 and 4 eV.

In the EE3 nanopowder, there is a luminescence band at 2.9 eV which contains both fast and slow emission components (Figure 14 a1). The excitation spectrum of 2.9 eV emission for a slow component resembles that of the $\alpha$-$Al_2O_3$ EE1 nanopowder recorded at 2.88 eV (Figure 12 a2), although the shoulder at 5.4 eV is more pronounced for $\gamma$-$Al_2O_3$ (Figure 14 a2). Based on the similarity of spectral features it is assigned to F-centre luminescence.

In the excitation spectra for the fast decay component of emissions at 3.2 eV and 4.1 eV, there are excitation bands at 5.8 and 7 eV and bands at 5.8, 6.3 and 7.2 eV, respectively. The main difference is the appearance of pronounced excitation band at 6.3 eV (Figure 14 a2 compare spectra depicted as dashed lines and symbols), which consist of the fast decay component. The decay recorded at 3.5 eV excited with 6.4 eV photons has two components 2.1 and 13.6 ns. Most probably the decay times obtained arise from the superposition of two different defect centres, which both have ns-range decay times. Namely, on the lower energy side $F^+_s$-centre and on higher energy side band the $F^+$-centre is contributing to the decay profile and emission spectra.

In the case of pure $\gamma$-$Al_2O_3$ FR3 in the excitation spectrum for 3 eV emission (Figure 14 b2 line), there are two major excitation bands at 5.4 and 6.0 eV. There are no features present at 7 eV like for FR1 and LV1, which is due to the fact that intrinsic absorption for $\gamma$-$Al_2O_3$ starts at 7.0 eV (see Section 7.1). Analogously to other transition alumina, this emission peaked at 3 eV is attributed to the $F^+_s$-centre. The excitation spectrum for 4.1 eV emission (Figure 14 b2

circles) shows also two excitation bands at 5.5 and 6.3 eV, which are located at the same place as for the sample FR2 (θ-$Al_2O_3$ containing sample). Analogously it is assigned to $F^+$-centre luminescence. It is also supported by luminescence decay studies, which revealed the following decay times for this band: 2.4 and 10.9 ns.

The fast component of 3 eV emission arising from the radiative decay of surface $F^+$-centre and the slow component is due to luminescence of the F-centre. The 4.1 eV band in $Al_2O_3$ FR3, emission band peaking at 3.6 eV and extending to 4 eV in $Al_2O_3$ EE3 is attributed to $F^+$-centre. This interpretation is also confirmed by other authors who have also attributed fast luminescence at 3.6 – 3.8 eV to $F^+$-centre in γ-$Al_2O_3$ (see Section 3 and [37, 38, 41])

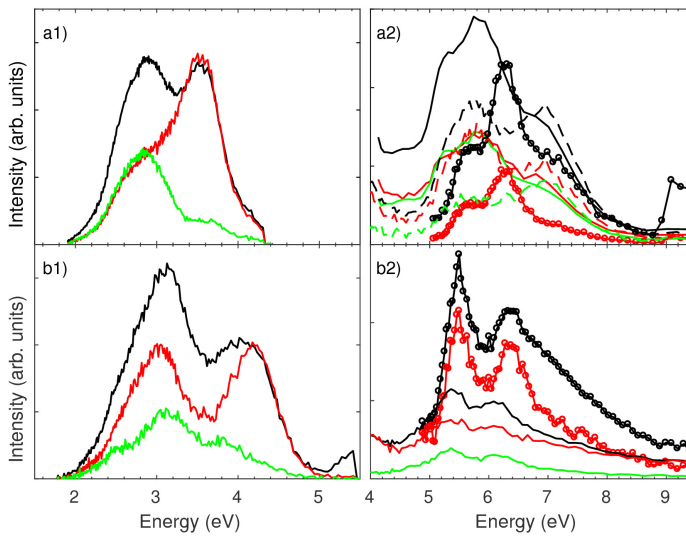


**Figure 14**. Emission and excitation spectra for nanopowders composed mainly of γ-$Al_2O_3$ at 8 K. Time-integrated (TI) – black, FTW – red and STW – green line, dashed line or symbols. Time window values were for FTW δt ≈ 2 ns and Δt ≈ 10 ns and for STW δt ≈ 100 ns and Δt ≈ 50 ns. a1) $Al_2O_3$ EE3 – emission spectrum excited with 5.2 eV photons; a2) excitation spectrum for 2.8 eV emission (lines), excitation spectrum for 3.2 eV emission (dashed line) and excitation spectrum for 4.1 eV emission (circles); b1) ultra-porous $Al_2O_3$ FR3 (γ-$Al_2O_3$) – emission spectrum excited with 6.4 eV photons; b2) excitation spectrum for 4 eV (circles) and 3 eV (lines) emission.

## Conclusion

The transition aluminas studied were produced by different methods and therefore in addition to the variation of phase composition, one could also expect the presence of a variety of defect centres. Based on luminescence studies there are mainly F-centre emitting near 3 eV, and $F^+$-centres near 3.8 eV present analogously to single crystals. Due to the nano-size of crystallites in the studied sample the surface $F_s^+$ are introduced as reported by Gorbunov et al. [42] in

γ- and δ-$Al_2O_3$ mixture. The luminescence of $F_s^+$-centres has nanosecond decay with emission peaked at 3 eV, which overlaps with ms emission of F-centres. It is also important to note that depending on the excitation energy the emission spectra of various defect centres overlap with intrinsic and impurity emission complicating the analysis of relaxation processes in transition alumina.

## 7.4 Impurity luminescence of alumina powders

Depending on the purity of chemicals used in the synthesis processes impurity ions in alumina play a role in the formation of optically active luminescence centres, which can be revealed by means of luminescence spectroscopy in excitation and emission spectra. The most common impurity ions found in alumina are the transition metals $Cr^{3+}$, $Fe^{2+}$, $Ti^{3+}$ etc. (see sections 2 and 3).

**$Cr^{3+}$ luminescence in $Al_2O_3$ LV1 and LV2 nanopowders**

The level of impurities in studied nanopowders varied due to different purity of raw materials used in synthesis. The lowest purity of initial starting chemicals (99.97%) was used for the preparation of the LV1 and LV2 alumina samples. In all other syntheses, the purity of raw materials was at least 99.99%. This means that stronger impurity ion effects were expected and revealed in $Al_2O_3$ LV1 and LV2 samples (Paper I). The most common impurity in alumina is usually $Cr^{3+}$ ions, which are responsible for the red colour of rubies. In the red region of emission spectra, the so-called R-lines of $Cr^{3+}$ ions are well-known. The R-lines designate the $^2E \rightarrow {}^4A_2$ electronic transition of $d^3$ configuration $Cr^{3+}$ ion. In α-$Al_2O_3$ these lines are at 694.3 and 692.9 nm [2]. The high-resolution spectra for $Al_2O_3$ LV1 and LV2 are presented in Figure 15a in the region of 650–900 nm. In these spectra, two spectral regions can be identified with different spectroscopic features. Around 680 to 720 nm there are narrow lines followed by a broad band extending until 900 nm. These lines are typical for the emission of impurity ions in oxide hosts. These samples were also studied in Tartu using X-ray photoelectron spectroscopy (XPS), which according to the setup specification can detect impurity metals in a concentration of the order of ≥0.1 at%, but no metal impurities were detected. An attempt to detect paramagnetic impurities like $Fe^{3+}$ ions showed that iron impurity was present in these nanopowders, which is not surprising because the EPR method is by several orders of magnitude more sensitive than XPS. In the $Al_2O_3$ LV1 luminescence spectrum the four strong lines at 682.7, 686.0, 689.5 and 691.5 nm were identified (Figure 15a). After the first set of lines, there are two less intensive lines at 701 and 705 nm. For the $Al_2O_3$ LV2 nanopowder the structure of the sharp lines is similar, only relative intensity of spectroscopic features is varying. There are four strong lines at 682.2, 685.7, 688.7 and 691 nm. At longer wavelengths, there are lines at 701.2 nm and 704.9 nm (Figure 15a). Previously, there have been reports for R doublet in θ-$Al_2O_3$. According to different authors [21,48,49], these lines are at 682.6 nm and 685.9 nm, which positions

correspond very well to spectral lines revealed in this work. In the studied LV samples, the R-lines corresponding to α-$Al_2O_3$ phase are not present. The two lines at 689 and 691 nm are tentatively assigned to the $Cr^{3+}$ ion at different site or to its emission in different alumina phase, e.g. δ-$Al_2O_3$, which is present in the LV samples according to XRD analysis. In α-$Al_2O_3$ also so-called N-lines around 701 and 705 nm [80] can be found, which correspond to emission from neighbouring pairs of $Cr^{3+}$ ions. Both LV nanopowders have also less intensive bands at these wavelengths, which can be caused by nearby situated $Cr^{3+}$ ions although in these samples the amount of $Cr^{3+}$ doping is less than 0.1 at% according to chemical analysis and therefore, the probability of neighbouring interacting ions should be low. Schawlow et.al [80] has shown that the emission bands of N-lines are detectable from around 0.2 at% concentration of $Cr^{3+}$.

According to the literature in more disordered δ- and γ-$Al_2O_3$ doped with $Cr^{3+}$ ions, one can observe an inhomogeneously broadened luminescence band around 700 nm [48,81]. The origin of broad emission band extending until 900 nm can be due to different impurity ions or centres formed in their participation. The EPR study shows that there are $Fe^{3+}$ ions present in $Al_2O_3$ LV1 and LV2 nanopowders. Thus, the long-wavelength wing can be explained by the interaction of octahedrally coordinated $Cr^{3+}$ ions with $Fe^{3+}$ impurities, which were shown to form an emission band at 770 nm [21]. The second factor causing the appearance of the broad band can be due to high disorder present in γ- and δ-$Al_2O_3$ [48]. The third possibility is $Fe^{3+}$ ion transition $^4T_1 \rightarrow {}^6A_1$ emission at 750 nm in nano-size alumina [40]. Probably in the studied samples the broad band is caused by all three circumstances. Different authors have also shown that increasing concentration of $Cr^{3+}$ ions cause a broad band at 770 nm and it has been interpreted by the formation of $Cr^{3+}$ clusters [47,82]. High concentration of $Cr^{3+}$ (around 1 at%) is a prerequisite to realise the creation of $Cr^{3+}$ clusters, which is not probable in LV samples, where this concentration is less than 0.1 at%.

**$Cr^{3+}$ luminescence in combustion synthesised nanopowders**

As was already mentioned, the $Al_2O_3$ EE1-EE4 nanopowders are of better purity due to high-quality chemicals used. The high-resolution emission spectra in the region of 690–700 nm are presented in Figure 15b. Nanopowders composed of γ-$Al_2O_3$ and α-$Al_2O_3$ mixtures in different ratios (EE3 85/15 and EE4 50/50 %, respectively) have larger linewidths for $Cr^{3+}$ R-lines compared to alumina single crystals and pure α-phase nanopowder (EE1) due to inhomogeneous line broadening. The main causes are crystallite size (being an average of 100 nm) and phase composition variation. Some influence of defects in crystallites cannot be excluded as well. Sample $Al_2O_3$ EE2 has a similar spectrum to α-$Al_2O_3$ single crystal, having R-lines and N-lines, which both are inhomogeneously broadened (Figure 15c). Also, it is possible to distinguish two lines of low intensity at 682 nm and 685 nm, which correspond to $Cr^{3+}$ in θ-$Al_2O_3$ (Figure 15c). This result shows a great advantage of the luminescence method, much higher sensitivity over XRD, which failed in detecting θ-$Al_2O_3$

phase in these samples due to its low concentration and because of overlap of diffraction lines with other alumina phases. A detected smaller shift of the R-lines for the sample $Al_2O_3$ EE3 is possibly due to a small amount of α-$Al_2O_3$ and smaller crystallite size.

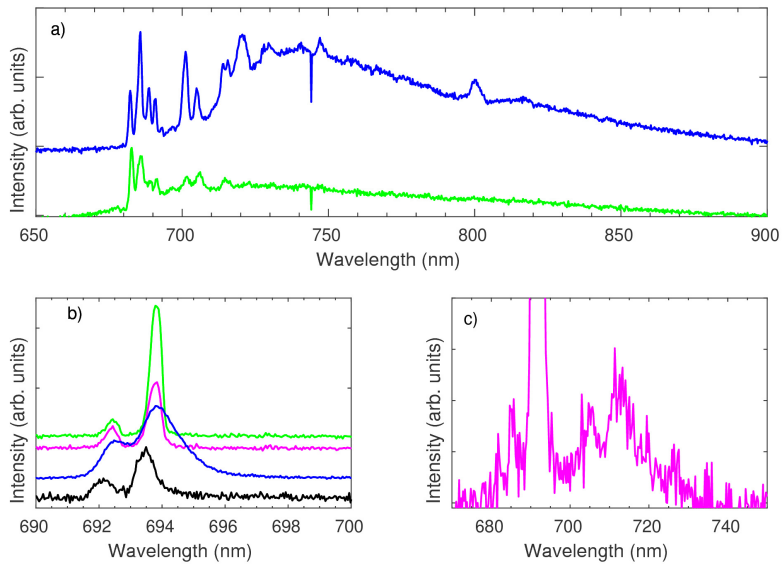


**Figure 15.** High-resolution emission spectra of $Cr^{3+}$ ions at 8K. a) Samples $Al_2O_3$ LV1 (blue) and $Al_2O_3$ LV2 (green) excited with 8.3 eV photons; b) Samples $Al_2O_3$ EE1 (green) and $Al_2O_3$ EE2 (magenta) excited with 11.3 eV photons. Samples $Al_2O_3$ EE3 (black) and $Al_2O_3$ EE4 (blue) excited with 5 keV electron beam. c) Zoom in to $Al_2O_3$ EE2 spectrum to show $Cr^{3+}$ lines corresponding to θ-$Al_2O_3$ phase (excited with 11.3 eV photons).

### Excitation spectra for $Cr^{3+}$ luminescence

Excitation spectra for $Cr^{3+}$ emission recorded at the R-line region are presented in Figure 16. The $Al_2O_3$ EE1 nanopowder has a strong excitation band with a maximum at 7 eV, which is interpreted as the $O^{2-}$ – $Cr^{3+}$ charge transfer (CT) band [25]. In the samples $Al_2O_3$ EE2 this CT band undergoes a red shift to 6.9 eV and in the $Al_2O_3$ EE4 to 6.7 eV. For sample $Al_2O_3$ EE3 it was not possible to record excitation spectrum for $Cr^{3+}$ centre emission due to very low luminescence intensity as it is mainly composed of γ-$Al_2O_3$. It shows that highly disordered structure and small crystallite size enhance non-radiative decay of electronic excitations. It is important to note that all combustion synthesised alumina with a considerable content of α-phase (varying from 100 to 40 %) have a well-defined host absorption onset at 8.9 eV. Therefore, the CT band is related to $Cr^{3+}$ ions substituted into the α-phase crystallites. This hypothesis is supported by negligible luminescence of $Cr^{3+}$ ions in γ-$Al_2O_3$. Hence, this shift

is correlated with the crystallite size as value decreases in a row of the $Al_2O_3$ EE1, EE2 and EE4 from 180 nm to 80 nm, respectively. Comparing excitation spectra luminescence of $Cr^{3+}$ ions in $Al_2O_3$ LV1 and $Al_2O_3$ LV2 nanopowders one can see that there is nearly no excitation band at 7 eV, but a well pronounced onset of intrinsic absorption at 7.5 eV for θ-$Al_2O_3$ in agreement with results described in section 7.1. It is not surprising because the CT band is characteristic of chromium ions in α-phase.

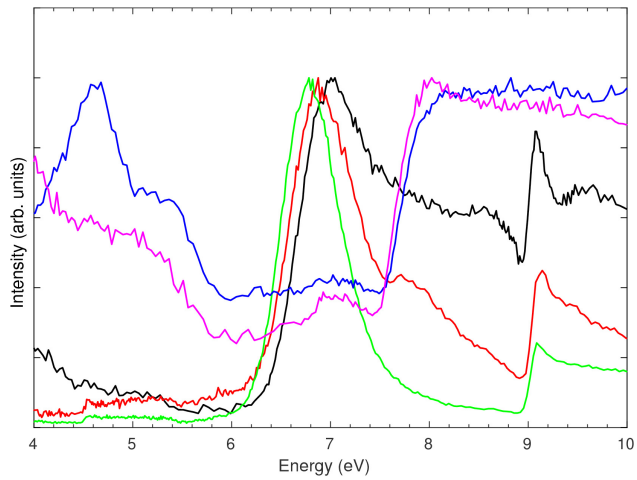


**Figure 16**. Excitation spectra for $Cr^{3+}$ emission at 1.8 eV (690 nm) at 8K. Black – $Al_2O_3$ EE1; red – $Al_2O_3$ EE2; green – $Al_2O_3$ EE4; blue – $Al_2O_3$ LV1 and magenta – $Al_2O_3$ LV2.

## Conclusion

In conclusion, the manifestation of transition metal ($Cr^{3+}$ and $Fe^{3+}$) impurity ions was investigated in different aluminas. In θ-$Al_2O_3$ the R-lines are shifted to shorter wavelengths due to changes in bond lengths resulting in stronger crystal field because of the crystal structure, which is different in comparison with α-$Al_2O_3$. The extra lines after the two strong R-lines can be caused by $Cr^{3+}$ occupying different sites in $AlO_4$ and $AlO_6$ structural units in these samples. Possibility to detect much smaller amounts of additional phases than by XRD in our samples using luminescence methods was demonstrated on the basis of θ-$Al_2O_3$.

# 8. DIAGNOSTICS OF ODS STEELS FOR HEAVY IRRADIATION ENVIRONMENT

Oxide dispersion-strengthened (ODS) steels are important construction materials used in harsh radiation environments at high temperatures like fission and fusion reactors in order to increase the thermal efficiency and safety margins [83]. The ODS steels are strengthened by the addition of nano-sized oxide crystallites, which are dispersed into the steel during the manufacturing process. The manufacturing process is well described in [84]. The inclusion of nanoparticles causes in such steels a complex microstructure (grain boundaries of oxide nanoparticles), which are expected to provide high temperature durability and promote recombination of point defects formed under irradiation and to trap transmutation products (He, H). These features appear to be very promising in increasing the radiation resistance of the structural materials for nuclear applications [85]. Recombination of defects formed in ODS steels during operation takes place presumably on the numerous internal interfaces originating from the presence of oxide ($Y_2O_3$, $Al_2O_3$, $Y_2Ti_2O_7$ etc) nanoparticles, but the atomistic mechanisms leading to this enhanced tolerance is still not well understood [86]. There is practically no information available regarding luminescence studies of ODS steels in literature, but luminescence methods due to its high sensitivity should offer an excellent tool to understand the role of these oxide nanocrystals and to investigate elementary processes of material damage on grain boundaries. The experiments planned were designed to show a potential of time-resolved luminescence spectroscopy in diagnostics of ODS steels.

The studied steel was called PM2000 and was produced by the PLANSEE GROUP and provided to our disposal by CIEMAT (Spain). PM2000 is a ferritic alloy, which contains mainly iron as well as aluminium, chromium, titanium and yttria additives (Table 8). The steel samples were cut into thin metal plates and cleaned using sandpaper and ultrasound bath in order to reduce contamination and influence of rough mechanical treatment.

**Table 8.** Chemical composition of PM2000 (wt%) [84]

| Cr | Ti | $Y_2O_3$ | Al | Fe |
|---|---|---|---|---|
| 20 | 0.5 | 0.5 | 5.5 | Bal |

The PM2000 steel sample was investigated using cathodoluminescence method in Tartu and applying low-temperature time-resolved luminescence spectroscopy at the beamlines I and BW3 under synchrotron radiation excitation in Hamburg. Results obtained are presented in Figures 17–19. In Figure 17 the emission spectrum under VUV excitation at 11.3 eV, which corresponds to the excitation of host absorption of all possible oxides (incl. $Al_2O_3$) in steels is

presented (red line). Revealed luminescence covers whole UV-visible range consisting of two broad bands peaked at 2.6 eV and 4.8 eV. As a comparison, the emission spectrum of pure $Y_2O_3$ powder is presented in Figure 17. One can observe that $Y_2O_3$ emission covers only part of the revealed luminescence in PM2000. It is important to note that yttria was the only oxide initially present in PM2000 steel. It means that other metal oxides are formed during the production process of the steel. The luminescence intensities were extremely low because of low concentration of oxide inclusions and a small penetration depths of VUV photons.

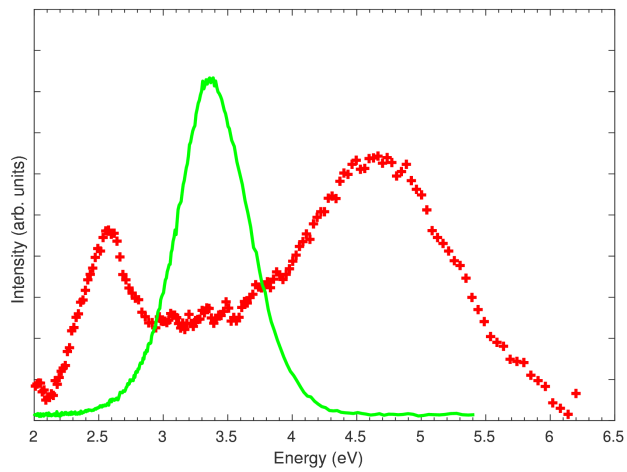


**Figure 17.** The emission spectrum of ODS steel at 7 K excited by 11.3 eV photons. PM2000 – red. $Y_2O_3$ (green) emission spectrum excited by 6.1 eV photons.

XUV photons are more suitable for these studies due to their larger penetration depth as the absorption coefficients are definitely below $10^6$ $cm^{-1}$ at intrinsic absorption edge of wide gap solids [61]. From the emission spectrum excited by XUV photons (Figure 18) two broad bands peaked at 7.6 eV and 4.6 eV were identified. The VUV emission band is STE emission of α-$Al_2O_3$ and the emission at 4.6 eV is similar to previously discussed radiative decay of triplet STE found in nano-size transition aluminas. The emission at 7.6 eV has a decay time of about 4 ns, which is similar to nano aluminas, but shorter than for single crystal (7 ns [28]) pointing to its small grain size. The decay curve is not exponential (Figure 18), which means a strong contribution from non-radiative channels e.g. decay of STEs at the grain boundaries of ODS steels.

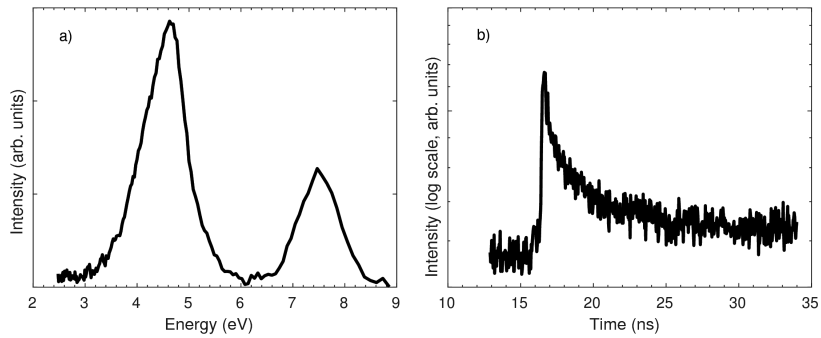


**Figure 18.** a) Emission spectrum of the PM2000 steel; b) Luminescence decay for 7.6 eV emission. Recorded at 8 K under excitation by 130 eV photons.

On the setups at the beamlines I and BW3 at DESY it is possible to record the decay times in nanosecond range, the 120 keV pulsed electron beam setup in Tartu was applied to study the slow decaying luminescence at 4.6 eV (Figure 19). Using deconvolution and fitting procedures the main decay component was found to be 1.4 μs and it is in agreement with earlier works on nanosize alumina [79]. This is similar emission like in samples in section 7.3 and this also points to triplet nature of the luminescence centre.

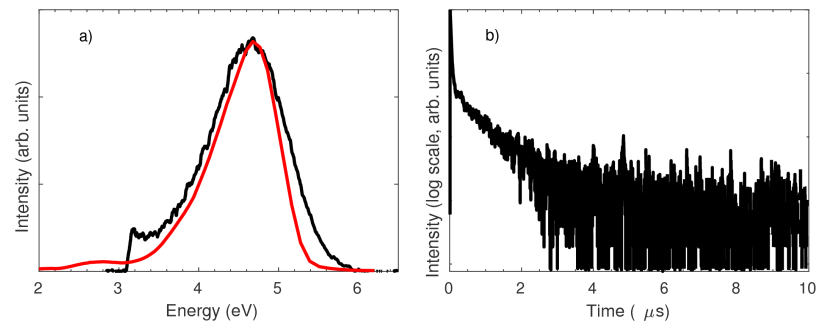


**Figure 19.** a) The emission spectrum of the PM2000 steel, excited by 120 keV pulsed electron-beam (black line) recorded at 78 K. Emission spectrum of alumina nanopowder containing different phases ($Al_2O_3$ EE2) recorded at 4 K (red line). b) Decay for 4.6 eV emission. Recorded at 78 K using excitation by pulsed 120 keV electron-beam.

In conclusion, the present work shows that using luminescence spectroscopy is applicable in diagnostics of ODS steels, aluminium and other oxides (incl. defects), which are formed in ODS steels during their production or radiation damage in harsh operation conditions. The intrinsic STE emission of $Al_2O_3$ has a shorter lifetime than in bulk single crystals due to non-radiative relaxation processes caused by OSD steel micro(nano)structure. The emission at 4.6 eV has characteristics similar to transition alumina i.e. the presence of other phases is not excluded.

# 9. SUMMARY

In this thesis, electronic and optical properties of nano-size α-$Al_2O_3$ and transition alumina phases (γ-, δ-, and θ-$Al_2O_3$) were studied using time-resolved luminescence spectroscopy at low temperatures under electron beam and synchrotron radiation excitation. A special attention was paid to the phase and crystallite size specific features in luminescence of alumina samples prepared with different synthesis methods. Synthesised samples were characterised using XRD, SEM and other methods to get information on crystallite size, phase composition and morphology of samples under investigation.

The main results from the work are following:

- Synthesis of samples was performed using combustion synthesis method, which allowed to obtain samples which have nano-size structure but are a mixture of different alumina phases. Other studied samples were obtained from colleagues in France and Latvia.
- The onset of intrinsic absorption energies for a mixture of δ- and θ-$Al_2O_3$ at 7.5 eV and γ-$Al_2O_3$ at 7 eV were determined. To our knowledge, these were the first measurements of γ-$Al_2O_3$ band gap value by luminescence methods.
- A revealed blue shift of the onset of intrinsic absorption for nanopowders in comparison with a single crystal of α-$Al_2O_3$ is attributed to residual stresses introduced during synthesis of nanocrystals.
- The introduction of $AlO_4$ structural units influences electronic structure of transition aluminas as well as formation of STE.
- Emission of triplet self-trapped excitons at 4.6 eV with slow 750–780 μs decay was found in nano-aluminas.
- Using the characteristic luminescence of $Cr^{3+}$ impurity in different phases of $Al_2O_3$ demonstrated the possibility to distinguish θ-$Al_2O_3$ phase in alumina samples with considerably higher sensitivity than with XRD. A determined red shift of charge transfer (O-Cr) band position to lower energies correlates with the decrease of crystallite size of α-$Al_2O_3$.
- As main defects F, $F^+$ and $F_s^+$-centre were identified and considerable similarities in their luminescence were demonstrated in all investigated nanopowders of different alumina phases.
- Luminescence spectroscopy under XUV and pulsed electron beam excitation has a strong potential in characterisation of oxide dispersion-strengthened (ODS) steels – to identify presence of optically active impurities, their phase composition, defects, and relaxation dynamics.

# 10. SUMMARY IN ESTONIAN

## Nanokristalse alumiiniumoksiidi α- ja üleminekufaaside uurimine VUV ja katoodluminestsentsi meetoditel

Käesolevas töös uuriti α-$Al_2O_3$ ja alumiiniumoksiidi üleminekufaaside (γ-, δ-, ja θ-$Al_2O_3$) nanokristallide elektroonseid ja optilisi omadusi kasutades aeglahutusega luminestsents-spektroskoopiat madalatel temperatuuridel. Eksperimendid viidi läbi kasutades elektronkiirt või sünkrotronkiirgust ergastusallikatena. Erilist tähelepanu pöörati faasikoostise ja kristalliidi suurusest tingitud nanopulbrite luminestsentsi iseärasustele alumiiniumoksiides, mis on sünteesitud erinevatel meetoditel. Sünteesitud objektide kristalliidi suuruse, faasikoostise ja morfoloogia kirjeldamiseks kasutati röntgendifraktsioonanalüüsi (XRD), skaneerivat elektronmikroskoopiat (SEM) ja teisi meetodeid.

Antud doktoritöö põhilised tulemused on järgnevad:

- Teostati objektide süntees kasutades kiiret põlemisreaktsiooni, mille käigus saadi objektid, mis olid nanokristalsed, aga sisaldasid mitut erinevat alumiiniumoksiidi faasist. Teised uuritud objektid valmistati Lätis ja Prantsusmaal meie koostööpartnerite poolt.
- Määrati omaneeldumise algus δ- ja θ-$Al_2O_3$ segu jaoks 7.5 eV juures ja γ-$Al_2O_3$ jaoks 7 eV juures. Meie teada on see esmakordne eksperimentaalne omaneeldumise alguse määramine γ-$Al_2O_3$ korral, kasutades luminestsents-spektroskoopiat.
- Analüüsiti omaneeldumise alguse sininihet nanopulbrites võrreldes monokristalliga. Nihke põhjustasid oletatavasti sünteesi käigus tekkinud pinged materjalis.
- $AlO_4$ struktuurielemendi lisandumine üleminekufaaside kristallstruktuuri mõjutab nende elektronstruktuuri ja iselõksustunud eksitoni formeerumist.
- Nanokristalses alumiiniumoksiidis leiti 4.6 eV juures aeglase 750–780 μs kustumisajaga tripletse iselõksustunud eksitoni kiirgus.
- Kasutades $Cr^{3+}$ lisanditsentri karakteristlikku kiirgust, näidati võimalust θ-$Al_2O_3$ faasi tuvastamiseks XRD analüüsist oluliselt suurema tundlikkusega. Samuti leiti (O-Cr) laenguülekandega seotud riba punanihe madalamatele energiatele, mis korreleerus α-$Al_2O_3$ kristalliidi suuruse vähenemisega.
- Näidati, et peamised defekti tsentrid on F, $F^+$ ja $F_s^+$-tsentrid ja nende luminestsents on uuritud erineva faasi koostisega nanopulbrites sarnane.
- Demonstreeriti ka luminestsents-spektroskoopia võimekust XUV ja elektronkiirega ergastusel rakenduslikult oluliste oksiid-dispersiooniga tugevdatud teraste koostise analüüsil.

# 11. ACKNOWLEDGEMENTS

I would like to thank my supervisors Dr. Marco Kirm and Dr. Eduard Feldbach for their guidance and support during my studies.

I would also like to thank Dr. Aarne Maaroos for the help of synthesising the samples and Dr. Eric Palcevskis (Latvia), Dr. Andrei Kanaev (Paris, France) and Dr. Rafael Vila (Madrid, Spain) for providing alumina samples studied by myself. I am grateful to Dr. Sebastian Vielhauer, Dr. Sergey Omelkov, Dr. Aleksei Kotlov (DESY, Hamburg, Germany), Dr. Hugo Mändar, Eliko Tõldsepp, Ivo Romet and others who helped to carry out different measurements in Tartu and Hamburg. I am thankful to Dr. Tiit Kärner and Dr. Viktor Seeman, who have shared their knowledge about electron paramagnetic resonance and helped to analyse collected data. All my fellow colleagues from the laboratory of physics of ionic crystals in Tartu are appreciated for their support.

I am grateful to my wife Ede, my parents, sister, and friends for encouraging me during these years.

Financial support was received from the Estonian Science Foundation (grant 8306), the Estonian Research Council (grant IUT-2-26), Estonian Materials Technology program project 3.2.1101.12-0014 „Synthesis, characterisation and application of activated rare-earth compounds in synthetic fuel synthesis reactors and other high-tech devices“, the European Community's Seventh Framework Programme (FP7/2007–2013 grants 226716, 312284) and is gratefully acknowledged. This work has been partially supported by Graduate School „Functional materials and technologies“, receiving funding from the European Social Fund under project 1.2.0401.09-0079 in Estonia. The work has been supported also by ASTRA project PER ASPERA, Graduate School of Functional Materials and Technologies, receiving funding from the European Regional Development Fund under project in University of Tartu, Estonia. I also acknowledge a partial financial support from the Estonian Centre of Excellence TK141 by the EU through the European Regional Development Fund (TK141 “Advanced materials and high-technology devices for sustainable energetics, sensorics and nanoelectronics”, project No. 2014-2020.4.01.15-0011). I appreciate the support of national scholarship program Kristjan Jaak managed by Archimedes Foundation in collaboration with the Ministry of Education and Research for providing travel grants.

# 12. REFERENCES


[1] M.A. Hines, G.D. Scholes, Colloidal PbS Nanocrystals with Size-Tunable Near-Infrared Emission: Observation of Post-Synthesis Self-Narrowing of the Particle Size Distribution, Adv. Mater. 15 (2003) 1844–1849.

[2] T.H. Maiman, Stimulated Optical Radiation in Ruby, Nature. 187 (1960) 493–494.

[3] D.R. Lide, ed., CRC Handbook of Chemistry and Physics, 89th ed., CRC Press, 2008.

[4] I. Levin, D. Brandon, Metastable Alumina Polymorphs: Crystal Structures and Transition Sequences, J. Am. Ceram. Soc. 81 (1998) 1995–2012.

[5] I. Levin, T. Gemming, D.G.G. Brandon, Some Metastable Polymorphs and Transient Stages of Transformation in Alumina, Phys. Status Solidi. 166 (1998) 197–218.

[6] Ľ. Smrčok, V. Langer, J. Křesťan, γ-Alumina: a single-crystal X-ray diffraction study, Acta Crystallogr. Sect. C Cryst. Struct. Commun. 62 (2006) i83–i84.

[7] L. Kovarik, M. Bowden, A. Genc, J. Szanyi, C.H.F. Peden, J.H. Kwak, Structure of δ-Alumina: Toward the Atomic Level Understanding of Transition Alumina Phases, J. Phys. Chem. C. 118 (2014) 18051–18058.

[8] G. Paglia, C. Buckley, A. Rohl, B. Hunter, R. Hart, J. Hanna, L. Byrne, Tetragonal structure model for boehmite-derived γ-alumina, Phys. Rev. B. 68 (2003) 144110.

[9] E. Menéndez-Proupin, G. Gutiérrez, Electronic properties of bulk γ-$Al_2O_3$, Phys. Rev. B. 72 (2005) 35116.

[10] A. Kirfel, K. Eichhorn, Accurate structure analysis with synchrotron radiation. The electron density in $Al_2O_3$ and $Cu_2O$, Acta Crystallogr. Sect. A Found. Crystallogr. 46 (1990) 271–284.

[11] Y. Repelin, E. Husson, Etudes structurales d'alumines de transition. I-alumines gamma et delta, Mater. Res. Bull. 25 (1990) 611–621.

[12] L. Kovarik, M. Bowden, D. Shi, N.M. Washton, A. Andersen, J.Z. Hu, J. Lee, J. Szanyi, J. Kwak, C.H.F. Peden, Unraveling the Origin of Structural Disorder in High Temperature Transition $Al_2O_3$: Structure of θ-$Al_2O_3$, Chem. Mater. 27 (2015) 7042–7049.

[13] J.M. McHale, Surface Energies and Thermodynamic Phase Stability in Nanocrystalline Aluminas, Science 277 (1997) 788–791.

[14] L.J. Sham, M. Schlüter, Density-functional theory of the energy gap, Phys. Rev. Lett. 51 (1983) 1888–1891.

[15] C.-K. Lee, E. Cho, H. Lee, K.S. Seol, S. Han, Comparative study of electronic structures and dielectric properties of alumina polymorphs by first-principles methods, Phys. Rev. B. 76 (2007) 245110.

[16] W.Y. Ching, Y. Xu, First-Principles Calculation of Electronic, Optical, and Structural Properties of alpha-$Al_2O_3$, J. Am. Ceram. Soc. 77 (1994) 404–411.

[17] K.S. Song, R.T. Williams, Self-Trapped Excitons, Springer Berlin Heidelberg, Berlin, Heidelberg, 1993.

[18] A.L. Shluger, K.P. McKenna, P.V. Sushko, D.M. Ramo, A. V Kimmel, Modelling of electron and hole trapping in oxides, Model. Simul. Mater. Sci. Eng. 17 (2009) 84004.

[19] J. Valbis, N. Itoh, Electronic excitations, luminescence and lattice defect formation in α-$Al_2O_3$ crystals, Radiat. Eff. Defects Solids. 116 (1991) 171–189.

[20] J. Aarik, A. Kasikov, M. Kirm, S. Lange, T. Uustare, H. Mändar, Optical properties of crystalline $Al_2O_3$ thin films grown by atomic layer deposition, Opt. Mater. Appl. Proc. SPIE, 2005: pp. 594601-594601–10.
[21] V.N. Snytnikov, V.O. Stoyanovskii, T.V. Larina, O.P. Krivoruchko, V.A. Ushakov, V.N. Parmon, Laser-induced luminescence of model $Fe/Al_2O_3$ and $Cr/Al_2O_3$ catalysts, Kinet. Catal. 49 (2008) 291–298.
[22] V. Singh, R.P.S. Chakradhar, J.L. Rao, K. Al-Shamery, M. Haase, Y.-D. Jho, Electron paramagnetic resonance and photoluminescence properties of α-$Al_2O_3:Cr^{3+}$ phosphors, Appl. Phys. B. 107 (2012) 489–495.
[23] M. Kirm, G. Zimmerer, E. Feldbach, A. Lushchik, C. Lushchik, F. Savikhin, Self-trapping and multiplication of electronic excitations in $Al_2O_3$ and $Al_2O_3$:Sc crystals, Phys. Rev. B. 60 (1999) 502–510.
[24] A.I. Surdo, V.S. Kortov, V.A. Pustovarov, Luminescence of F and $F^+$ centers in corundum upon excitation in the interval from 4 to 40 eV, Radiat. Meas. 33 (2001) 587–591.
[25] V.N. Makhov, A. Lushchik, C.B. Lushchik, M. Kirm, E. Vasil'chenko, S. Vielhauer, V.V. Harutunyan, E. Aleksanyan, Luminescence and radiation defects in electron-irradiated $Al_2O_3$ and $Al_2O_3$:Cr, Nucl. Instruments Methods Phys. Res. Sect. B Beam Interact. with Mater. Atoms. 266 (2008) 2949–2952.
[26] L. Trinkler, B. Berzina, D. Jakimovica, J. Grabis, I. Steins, UV-light induced luminescence processes in $Al_2O_3$ bulk and nanosize powders, Opt. Mater. 32 (2010) 789–795.
[27] M. Kirm, V. Harutunyan, V. Makhov, S. Vielhauer, VUV luminescence of as-grown and electron irradiated corundum single crystals, Opt. Mater. Appl. Proc. SPIE, 2005: pp. 594606-594606–6.
[28] A. Lushchik, M. Kirm, C. Lushchik, I. Martinson, G. Zimmerer, Luminescence of free and self-trapped excitons in wide-gap oxides, J. Lumin. 87 (2000) 232–234.
[29] V. Babin, E. Feldbach, M. Kirm, V.N. Makhov, S. Vielhauer, Deep VUV scintillators for detectors working in cryogenic environment, IEEE Trans. Nucl. Sci. 55 (2008) 1437–1444.
[30] L. Museur, M. Bouslama, M. Amamra, A. Kanaev, Electronic transitions in α, θ and γ polymorphs of ultraporous monolithic alumina, Phys. Status Solidi – Rapid Res. Lett. 4 (2013) 5–6.
[31] M. Kirm, A. Lushchik, C. Lushchik, Creation of groups of spatially correlated excitations in wide-gap solids, Phys. Status Solidi. 202 (2005) 213–220.
[32] B.D. Evans, G.J. Pogatshnik, Y. Chen, Optical properties of lattice defects in α-$Al_2O_3$, Nucl. Instruments Methods Phys. Res. Sect. B Beam Interact. with Mater. Atoms. 91 (1994) 258–262.
[33] B.D. Evans, M. Stapelbroek, Optical properties of the $F^+$ center in crystalline $Al_2O_3$, Phys. Rev. B. 18 (1978) 7089–7098.
[34] M. Itou, A. Fujiwara, T. Uchino, Reversible photoinduced interconversion of color centers in α-$Al_2O_3$ prepared under vacuum, J. Phys. Chem. C. 113 (2009) 20949–20957.
[35] A.I. Surdo, V.A. Pustovarov, V.S. Kortov, A.S. Kishka, E.I. Zinin, Luminescence in anion-defective crystals over the nano-, micro- and millisecond intervals, Nucl. Instruments Methods Phys. Res. Sect. A Accel. Spectrometers, Detect. Assoc. Equip. 543 (2005) 234–238.
[36] M.J. Springis, J.A. Valbis, Visible Luminescence of Colour Centres in Sapphire, Phys. Status Solidi. 123 (1984) 335–343.

[37] S. Liu, L. Zhang, Y. Fan, J. Luo, P. Zhang, L. An, Ultraviolet irradiation-induced photoluminescence degradation in γ-alumina nanoparticles, Appl. Phys. Lett. 89 (2006) 51911.
[38] G. Pozina, D.H. Trinh, H. Högberg, M. Collin, I. Reineck, L. Hultman, Phase identification in γ- and κ-alumina coatings by cathodoluminescence, Scr. Mater. 61 (2009) 379–382.
[39] M. Baronskiy, A. Rastorguev, A. Zhuzhgov, A. Kostyukov, O. Krivoruchko, V. Snytnikov, Photoluminescence and Raman spectroscopy studies of low-temperature γ-$Al_2O_3$ phases synthesized from different precursors, Opt. Mater. 53 (2016) 87–93.
[40] L. Trinkler, B. Berzina, Z. Jevsjutina, J. Grabis, I. Steins, C.J. Baily, Photoluminescence of $Al_2O_3$ nanopowders of different phases, Opt. Mater. 34 (2012) 1553–1557.
[41] V.S. Kortov, S.V. Zvonarev, A.I. Medvedev, Pulsed cathodoluminescence of nanoscale aluminum oxide with different phase compositions, J. Lumin. 131 (2011) 1904–1907.
[42] S.V. Gorbunov, S.O. Cholakh, V.A. Pustovarov, V.Y. Yakovlev, A.F. Zatsepin, A.I. Kucharenko, Electronic excitations and intrinsic defects in nanostructural $Al_2O_3$, Phys. Status Solidi. 2 (2005) 351–354.
[43] S.V. Bulyarskii, A.E. Kozhevin, S.N. Mikov, V.V. Prikhodko, Anomalous R-Line Behaviour in Nanocrystalline $Al_2O_3$:$Cr^{3+}$, Phys. Status Solidi. 180 (2000) 555–560.
[44] V.A. Pustovarov, V.S. Kortov, S.V. Zvonarev, A.I. Medvedev, Luminescent vacuum ultraviolet spectroscopy of $Cr^{3+}$ ions in nanostructured aluminum oxide, J. Lumin. 132 (2012) 2868–2873.
[45] D. Renusch, M. Grimsditch, J.D. Jorgensen, J.P. Hodges, Pressure Dependence of $Cr^{3+}$ Fluorescence in theta-Alumina, Oxid. Met. 56 (2001) 299–311.
[46] A. Rastorguev, M. Baronskiy, A. Zhuzhgov, A. Kostyukov, O. Krivoruchko, V. Snytnikov, Local structure of low-temperature γ-$Al_2O_3$ phases as determined by the luminescence of $Cr^{3+}$ and $Fe^{3+}$, RSC Adv. 5 (2015) 5686–5694.
[47] S.P. Jamison, G.F. Imbusch, Temperature dependence of the luminescence from heavily doped ruby, J. Lumin. 75 (1997) 143–147.
[48] V.N. Snytnikov, V.O. Stoyanovskii, V.A. Ushakov, V.N. Parmon, Luminescence of $Al_2O_3$ crystal modifications excited by the ArF excimer laser, Kinet. Catal. 46 (2005) 260–268.
[49] Q. Wen, D.M. Lipkin, D.R. Clarke, Luminescence Characterization of Chromium-Containing θ-Alumina, J. Am. Ceram. Soc. 81 (1998) 3345–3348.
[50] B.F. Gächter, J.A. Koningstein, Zero phonon transitions and interacting Jahn-Teller phonon energies from the fluorescence spectrum of α-$Al_2O_3$:$Ti^{3+}$, J. Chem. Phys.60 (1974) 2003-2006.
[51] P. Moulton, Ti-doped sapphire: tunable solid-state laser, Opt. News. 8 (1982) 1982.
[52] A. van Die, A.C.H.I. Leenaers, W.F. van der Weg, G. Blasse, A search for luminescence of the trivalent manganese ion in solid aluminates, Mater. Res. Bull. 22 (1987) 781–788.
[53] L. Favaro, A. Boumaza, P. Roy, J. Lédion, G. Sattonnay, J.B. Brubach, A.M. Huntz, R. Tétot, Experimental and ab initio infrared study of χ-, κ- and α-aluminas formed from gibbsite, J. Solid State Chem. 183 (2010) 901–908.

[54] W. Ching, L. Ouyang, P. Rulis, H. Yao, Ab initio study of the physical properties of γ-$Al_2O_3$: Lattice dynamics, bulk properties, electronic structure, bonding, optical properties, and ELNES/XANES spectra, Phys. Rev. B. 78 (2008) 14106.
[55] C. Loyola, E. Menéndez-Proupin, G. Gutiérrez, Atomistic study of vibrational properties of γ-$Al_2O_3$, J. Mater. Sci. 45 (2010) 5094–5100.
[56] S.-D. Mo, Y. Xu, W.-Y. Ching, Electronic and Structural Properties of Bulk γ-$Al_2O_3$, J. Am. Ceram. 80 (1997) 1193–1197.
[57] S.-D. Mo, W. Ching, Electronic and optical properties of θ-$Al_2O_3$ and comparison to α-$Al_2O_3$, Phys. Rev. B. 57 (1998) 15219–15228.
[58] I.P. Batra, Electronic structure of α-$Al_2O_3$, J. Phys. C Solid State Phys. 15 (1982) 5399–5410.
[59] E. Feldbach, E. Tõldsepp, M. Kirm, A. Lushchik, K. Mizohata, J. Räisänen, Radiation resistance diagnostics of wide-gap optical materials, Opt. Mater. 55 (2016) 164–167.
[60] O. Bjorneholm, F. Federmann, C. Larsson, U. Hahn, A. Rieck, S. Kakar, T. Möller, A. Beutler, F. Fössing, Performance of the extreme ultraviolet high resolution undulator beamline BW3 at Hasylab: First results and time-of-flight spectroscopy, Rev. Sci. Instrum. 66 (1995) 1732.
[61] M. Kirm, A. Lushchik, C. Lushchik, S. Vielhauer, G. Zimmerer, Luminescence of pure and doped $Al_2O_3$ and MgO single crystals under inner-shell excitation, J. Lumin. 102–103 (2003) 307–312.
[62] G. Zimmerer, SUPERLUMI: A unique setup for luminescence spectroscopy with synchrotron radiation, Radiat. Meas. 42 (2007) 859–864.
[63] V. Kisand, Creation of free excitons in solid krypton investigated by time-resolved luminescence spectroscopy, University of Hamburg, 2001.
[64] M. True, Fine structure in d-f and f-f transitions of $Tm^{3+}$ and systematic investigation of $3d_5$ – $3d^44s$ absorption of $Mn^{2+}$ doped fluorides, University of Hamburg, 2004.
[65] E. Negodine, Inter- and intraconfigurational luminescence of $LiYF_4$:$Er^{3+}$ under selective VUV excitation, University of Hamburg, 2003.
[66] S. Vielhauer, Innerschalenanregungen und sekundäre Exzitonen in Edelgasfestkörpern, University of Hamburg, 2003.
[67] J.A. Rodríguez, M. Fernández-García, eds., Synthesis, Properties, and Applications of Oxide Nanomaterials, John Wiley & Sons, Inc., Hoboken, NJ, USA, 2007.
[68] J. Kakos, L. Baca, P. Veis, L. Pach, Photoluminescence Spectra and Crystallization of θ-$Al_2O_3$ and α-$Al_2O_3$ from AlOOH-Fe$(NO_3)_3$ Gels, J. Sol-Gel Sci. Technol. 21 (2001) 167–172.
[69] Y.A. Kotov, Electric Explosion of Wires as a Method for Preparation of Nanopowders, J. Nanoparticle Res. 5 (2003) 539–550.
[70] J. Grabis, A. Kuzjukevics, D. Rasmane, M. Mogensen, S. Linderoth, Perparation of nanocrystalline YSZ powders by the plasma technique, J. Mater. Sci. 33 (1998) 723–728.
[71] R. Ianoş, I. Lazău, C. Păcurariu, The influence of combustion synthesis conditions on the α-$Al_2O_3$ powder preparation, J. Mater. Sci. 44 (2009) 1016–1023.
[72] J.-L. Vignes, C. Frappart, T. Di Costanzo, J.-C. Rouchaud, L. Mazerolles, D. Michel, Ultraporous monoliths of alumina prepared at room temperature by aluminium oxidation, J. Mater. Sci. 43 (2008) 1234–1240.

[73] X. Mi, X. Zhang, X. Ba, Z. Bai, L. Lu, X. Wang, Q. Liu, Preparation and luminescent properties of $Cr^{3+}$:$Al_2O_3$ nano-powders by low-temperature combustion synthesis, Adv. Powder Technol. 20 (2009) 164–168.
[74] M. Pavese, S. Biamino, Mesoporous alumina obtained by combustion synthesis without template, J. Porous Mater. 16 (2007) 59–64.
[75] Y. Wang, N. Herron, Nanometer-sized semiconductor clusters: materials synthesis, quantum size effects, and photophysical properties, J. Phys. Chem. 95 (1991) 525–532.
[76] M. Kodu, T. Avarmaa, R. Jaaniso, K. Leemets, H. Mändar, V. Nagirnyi, Pulsed laser deposition of $CdWO_4$ thin films, Superlattices Microstruct. 98 (2016) 18–28.
[77] H. Song, R.H. French, R.L. Coble, Effect of Residual Strain on the Electronic Structure of Alumina and Magnesia, J. Am. Ceram. Soc. 72 (1989) 990–994.
[78] E. Tõldsepp, F. Schoenstein, M. Amamra, R. Saar, E. Feldbach, A. Kanaev, M. Kirm, Spark plasma sintering of ultra-porous γ-$Al_2O_3$, Ceram. Int. 42 (2016) 11709–11715.
[79] V.S. Kortov, A.E. Ermakov, A.F. Zatsepin, M.A. Uĭmin, S.V. Nikiforov, A.A. Mysik, V.S. Gaviko, Specific features of luminescence properties of nanostructured aluminum oxide, Phys. Solid State. 50 (2008) 957–961.
[80] A.L. Schawlow, D.L. Wood, A.M. Clogston, Electronic Spectra of Exchange-Coupled Ion Pairs in Crystals, Phys. Rev. Lett. 3 (1959) 271–273.
[81] C. Pan, S.Y. Chen, P. Shen, Photoluminescence and transformation of dense $Al_2O_3$:$Cr^{3+}$ condensates synthesized by laser-ablation route, J. Cryst. Growth. 310 (2008) 699–705.
[82] T. Toyoda, T. Obikawa, T. Shigenari, Photoluminescence spectroscopy of $Cr^{3+}$ in ceramic $Al_2O_3$, Mater. Sci. Eng. B. 54 (1998) 33–37.
[83] G.R. Odette, M.J. Alinger, B.D. Wirth, Recent Developments in Irradiation-Resistant Steels, Annu. Rev. Mater. Res. 38 (2008) 471–503.
[84] C. Capdevila, Y.L. Chen, A.R. Jones, H.K.D.H. Bhadeshia, Grain Boundary Mobility in Fe-Base Oxide Dispersion Strengthened PM2000 Alloy, ISIJ Int. 43 (2003) 777–783.
[85] S.J. Zinkle, J.T. Busby, Structural materials for fission & fusion energy, Mater. Today. 12 (2009) 12–19.
[86] X.-M.M. Bai, A.F. Voter, R.G. Hoagland, M. Nastasi, B.P. Uberuaga, Efficient annealing of radiation damage near grain boundaries via interstitial emission., Science. 327 (2010) 1631–4.

# 13. PUBLICATIONS

# CURRICULUM VITAE


**Name:** Marek Oja
**Date of birth:** June 25, 1986
**Citizenship:** Estonian
**Address:** Institute of Physics, University of Tartu, W. Ostwald Str 1, 50411, Estonia
**E-mail:** marek.oja@ut.ee


**Current position:** Laboratory of Physics of Ionic Crystals, Institute of Physics, University of Tartu, Junior Research Fellow of Solid State Physics

**Education:**

| | |
|---|---|
| 2009–2011 | University of Tartu, MSc in Physics |
| 2005–2009 | University of Tartu, BSc in Physics, cum laude |
| 2002–2005 | Hugo Treffner Gymnasium |

**Language skills:** Estonian (mother tongue), English (very good), German (good), French (basic), Swedish (basic)

**Institution and position held:**

| | |
|---|---|
| 2015– | University of Tartu, Faculty of Science and Technology, Institute of Physics, Laboratory of Physics of Ionic Crystals, Junior Research Fellow of Solid State Physics |
| 2015– | Software Technology and Applications Competence Centre, Researcher |
| 2011–2015 | University of Tartu, Faculty of Science and Technology, Institute of Physics, Laboratory of Physics of Ionic Crystals, engineer |

**Research interests:**
Electronic structure and properties of wide band gap materials using luminescence and electron paramagnetic resonance research methods.

**Publications:**


**M. Oja**, E. Tõldsepp, E. Feldbach, H. Mägi, S. Omelkov, M. Kirm, Luminescence Study of Alumina Nanopowders Prepared by Various Methods, *Radiation Measurements* **90** (2016) 75–79.

**M. Oja**, E. Feldbach, A. Kotlov, H. Mändar, S. Vielhauer and M. Kirm, Intrinsic and Extrinsic Luminescence of Nanosize Transition Alumina Powders, *Radiation Measurements* **56** (2013) 411–414.

E. Feldbach, T. Avarmaa, V. Denks, H. Mägi, **M. Oja**, E. Tõldsepp, M. Kirm, Tuning the electronic properties of naturally nanostructured compounds, *Physica Scripta*, **T157** (2013) 014013.

M. Kirm, E. Feldbach, A. Kotlov, P. Liblik, A. Lushchik, **M. Oja**, E. Palcevskis, VUV spectroscopy and electronic excitations in nano-size alumina, *Radiation Measurements*, **45** (2010) 618–620.

**Conference presentations:**

**M. Oja**, E. Feldbach, M. Kirm, "F and $F^+$ centre luminescence in alumina nanopowders". Poster presentation at the International Conference Functional Materials and Nanotechnologies-2017, 2017, Tartu, Estonia.

**M. Oja**, E. Feldbach, M. Kirm, "F and $F^+$ centre luminescence in alumina nanopowders". Poster presentation at the Functional Materials and Technologies Graduate School Conference, 2017, Tartu, Estonia.

**M. Oja,** E. Tõldsepp, E. Feldbach, M. Amamra, A. Kanaev, H. Mägi, S. Omelkov, F. Schoenstein, M. Kirm "Luminescence study of alumina nanopowders and ceramics prepared by spark plasma sintering method". Poster presentation at the 9th International Conference on Luminescent Detectors and Transformers of Ionizing Radiation (LUMDETR), 2015, Tartu, Estonia.

**M. Oja**, E. Feldbach, M. Kirm, A. Lushchik, S. Omelkov, R. Vila, P. Fernandez, A. Kotlov. "Luminescence study of ODS steels". Poster presentation at the 17th International Conference on Luminescence, 2014, Wroclaw, Poland.

**M. Oja**, E. Tõldsepp, T. Kärner, E. Feldbach, M. Kirm, "EPR spectroscopy of C3A". Poster presentation at the Functional Materials and Technologies Graduate School Conference, 2014, Tartu, Estonia.

**M. Oja**, E. Tõldsepp, T. Kärner, E. Feldbach, M. Kirm, "EPR spectroscopy of $Ca_3Al_2O_6$ (C3A)". Poster presentation at the 9th International Conference Functional Materials and Nanotechnologies, 2014, Riga, Latvia.

**M. Oja**, E. Feldbach, H. Mägi, E. Tõldsepp, A. Dindune, E. Palcevskis, M. Kirm, "Luminescence spectroscopy of pure, Mn- and Mg-doped Ca-phosphate apatites". Poster presentation at the Fourth International Workshop on Advanced Spectroscopy and Optical Materials, 2013, Gdansk, Poland.

**M. Oja,** E. Feldbach, M. Kirm, "Electronic excitations of ultra-porous alumina". Poster presentation at the Functional Materials and Technologies Graduate School Conference, 2013, Tallinn, Estonia.

**M. Oja**, E. Feldbach, M. Kirm, L. Museur, M. Amamra, A. Kanaev, "Luminescence studies of ultra-porous alumina nanopowders". Poster presentation at the 8th International Conference Functional Materials and Nanotechnologies, 2013, Tartu, Estonia.

**M. Oja**, E. Feldbach, A. Kotlov, H. Mändar, S. Vielhauer, M. Kirm "Intrinsic and extrinsic luminescence of nanosize transition alumina powders". Poster presentation at the 8th International Conference on Luminescent Detectors and Transformers of Ionizing Radiation (LUMDETR), 2012, Halle, Germany.

**M. Oja,** E. Feldbach, S. Vielhauer, M. Kirm, "Electronic properties of transition alumina nanopowders investigated by means of VUV and cathodo-

luminescence spectroscopy". Poster presentation at the Functional Materials and Technologies Graduate School Conference, 2012, Tartu, Estonia.

**M. Oja**, E. Feldbach, M. Kirm, P. Liblik, A. Lushchik, E. Palcevskis, "Luminescence spectroscopy of nano-size alumina", Poster presentation at the International Conference Functional Materials and Nanotechnologies, 2009, Riga, Latvia

**Awards and scholarships:**

2017 Dora Plus short study visits travel scholarship to attend the 20th Meeting of the International Society of Magnetic Resonance

2013 Kristjan Jaak's program scholarship to attend The Fourth International Workshop on Advanced Spectroscopy and Optical Materials

2013 Functional Materials and Technologies Graduate School travel scholarship to attend 6th EFEPR Winter School on Advanced EPR Spectroscopy

2012 Kristjan Jaak's program scholarship to attend the 8th International Conference on Luminescent Detectors and Transformers of Ionizing Radiation (LUMDETR)

2011 University of Tartu, Institute of Physics student scholarship

2009 University of Tartu, Institute of Physics student scholarship

**Other activities and membership:**

Member of Akadeemiake editorial board from 2016

**Courses attended:**

Bruker training course "Continous Wave EPR" 09.03 – 11.03.2016, Rheinstetten, Germany

Maxlab training course "EXAFS for beginners" 08.09 – 18.09.2014, Lund, Sweden

6th EFEPR Winter School on Advanced EPR Spectroscopy, 12.01 – 18.01. 2013, Rehovot, Israel

DESY Summer Student Programme 2009, 21.07 – 10.09.2009, Hamburg, Germany

# ELULOOKIRJELDUS


| | |
|---|---|
| **Nimi:** | Marek Oja |
| **Sünniaeg:** | 25. juuni, 1986 |
| **Kodakondsus:** | Eesti |
| **Aadress:** | Füüsika Instituut, Tartu Ülikool, W. Ostwaldi tn 1, 50411, Tartu |
| **E-post:** | marek.oja@ut.ee |

**Praegune töökoht:** Ioonkristallide füüsika labor, Füüsika Insituut, Tartu Ülikool, nooremteadur


**Haridus:**

| | |
|---|---|
| 2009 – 2011 | Tartu Ülikool, loodusteaduste magister (MSc), füüsika |
| 2005 – 2009 | Tartu Ülikool, loodusteaduste bakalaureuse kraad (BSc), füüsika, cum laude |
| 2002 – 2005 | Tartu Hugo Treffneri Gümnaasium |

**Keelteoskus:** eesti (emakeel), inglise (väga hea), saksa (hea), prantsuse (baasteadmised), rootsi (baasteadmised)

**Töökogemus:**

| | |
|---|---|
| 2015– | Tartu Ülikool, Füüsika Instituut, Ioonkristallide füüsika labor, tahkisefüüsika nooremteadur |
| 2015– | OÜ Tarkvara Tehnoloogia Arenduskeskus, teadur |
| 2011–2015 | Tartu Ülikool, Füüsika Insituut, Ioonkristallide füüsika labor, insener |

**Peamised uurimisvaldkonnad:**
Laia keelutsooniga materjalide elektroonsete omaduste uurimine kasutades luminestsentsspektroskoopia ja elektron paramagneetilist resonantsi meetodeid.

**Publikatsioonid:**


**M. Oja**, E. Tõldsepp, E. Feldbach, H. Mägi, S. Omelkov, M. Kirm, Luminescence Study of Alumina Nanopowders Prepared by Various Methods, *Radiation Measurements* **90** (2016) 75–79.

**M. Oja**, E. Feldbach, A. Kotlov, H. Mändar, S. Vielhauer and M. Kirm, Intrinsic and Extrinsic Luminescence of Nanosize Transition Alumina Powders, *Radiation Measurements* **56** (2013) 411–414.

E. Feldbach, T. Avarmaa, V. Denks, H. Mägi, **M. Oja**, E. Tõldsepp, M. Kirm, Tuning the electronic properties of naturally nanostructured compounds, *Physica Scripta*, **T157** (2013) 014013.

M. Kirm, E. Feldbach, A. Kotlov, P. Liblik, A. Lushchik, **M. Oja**, E. Palcevskis, VUV spectroscopy and electronic excitations in nano-size alumina, *Radiation Measurements*, **45** (2010) 618–620.

**Konverentsiettekanded:**

**M. Oja**, E. Feldbach, M. Kirm, "F and $F^+$ centre luminescence in alumina nanopowders". Stendiettekanne rahvusvahelisel konverentsil "Functional Materials and Nanotechnologies-2017", 2017, Tartu, Estonia.

**M. Oja**, E. Feldbach, M. Kirm, "F and $F^+$ centre luminescence in alumina nanopowders". Stendiettekanne Funktsionaalsete materjalide ja tehnoloogiate doktorikooli konverentsil, 2017, Tartu, Eesti.

**M. Oja,** E. Tõldsepp, E. Feldbach, M. Amamra, A. Kanaev, H. Mägi, S. Omelkov, F. Schoenstein, M. Kirm "Luminescence study of alumina nanopowders and ceramics prepared by spark plasma sintering method". Stendiettekanne konverentsil "9th International Conference on Luminescent Detectors and Transformers of Ionizing Radiation (LUMDETR)", 2015, Tartu, Eesti.

**M. Oja**, E. Feldbach, M. Kirm, A. Lushchik, S. Omelkov, R. Vila, P. Fernandez, A. Kotlov. "Luminescence study of ODS steels". Stendiettekanne konverentsil "17th International Conference on Luminescence", 2014, Wroclaw, Poola.

**M. Oja**, E. Tõldsepp, T. Kärner, E. Feldbach, M. Kirm, "EPR spectroscopy of C3A". Stendiettekanne Funktsionaalsete materjalide ja tehnoloogiate doktorikooli konverentsil, 2014, Tartu, Eesti.

**M. Oja**, E. Tõldsepp, T. Kärner, E. Feldbach, M. Kirm, "EPR spectroscopy of $Ca_3Al_2O_6$ (C3A)". Stendiettekanne konverentsil "9th International Conference Functional Materials and Nanotechnologies", 2014, Riga, Läti.

**M. Oja**, E. Feldbach, H. Mägi, E. Tõldsepp, A. Dindune, E. Palcevskis, M. Kirm, "Luminescence spectroscopy of pure, Mn- and Mg-doped Ca-phosphate apatites". Stendiettekanne konverentsil "Fourth International Workshop on Advanced Spectroscopy and Optical Materials", 2013, Gdansk, Poola.

**M. Oja,** E. Feldbach, M. Kirm, "Electronic excitations of ultra-porous alumina". Stendiettekanne Funktsionaalsete materjalide ja tehnoloogiate doktorikooli konverentsil, 2013, Tallinn, Eesti.

**M. Oja**, E. Feldbach, M. Kirm, L. Museur, M. Amamra, A. Kanaev, "Luminescence studies of ultra-porous alumina nanopowders". Stendiettekanne konverentsil "8th International Conference Functional Materials and Nanotechnologies", 2013, Tartu, Eesti.

**M. Oja**, E. Feldbach, A. Kotlov, H. Mändar, S. Vielhauer, M. Kirm "Intrinsic and extrinsic luminescence of nanosize transition alumina powders". Stendiettekanne konverentsil "8th International Conference on Luminescent Detectors and Transformers of Ionizing Radiation (LUMDETR)", 2012, Halle, Saksamaa.

**M. Oja,** E. Feldbach, S. Vielhauer, M. Kirm, "Electronic properties of transition alumina nanopowders investigated by means of VUV and cathodoluminescence spectroscopy". Stendiettekanne Funktsionaalsete materjalide ja tehnoloogiate doktorikooli konverentsil, 2012, Tartu, Eesti.

**M. Oja**, E. Feldbach, M. Kirm, P. Liblik, A. Lushchik, E. Palcevskis, "Luminescence spectroscopy of nano-size alumina", Stendiettekanne konverentsil

"International Conference Functional Materials and Nanotechnologies", 2009, Riga, Läti

**Saadud uurimistoetused ja stipendiumid:**

2017 Dora Plus Lühiajalise õpirände toetus konverentsi "20th Meeting of the International Society of Magnetic Resonance" osalemiseks

2013 Kristjan Jaagu välissõidu stipendium konverentsil "The Fourth International Workshop on Advanced Spectroscopy and Optical Materials" osalemiseks

2013 Funktsionaalsete materjalide ja tehnoloogiate doktorikooli reisistipendium osalemiseks talvekoolis "EFEPR Winter School on Advanced EPR Spectroscopy"

2012 Kristjan Jaagu välissõidu stipendium konverentsil "The 8th International Conference on Luminescent Detectors and Transformers of Ionizing Radiation (LUMDETR)" osalemiseks

2011 Tartu Ülikool, Füüsika Instituudi tudengistipendium

2009 Tartu Ülikool, Füüsika Instituudi tudengistipendium

**Muu teaduslik organisatsiooniline ja erialane tegevus:**

"Akadeemiakese" kolleegiumi liige alates 2016

**Osalemine kursustel:**

Brukeri koolitus "Continous Wave EPR" 09.03 – 11.03.2016, Rheinstetten, Saksamaa

Maxlab koolitus "EXAFS for beginners" 08.09 – 18.09.2014, Lund, Rootsi

Talvekool "6th EFEPR Winter School on Advanced EPR Spectroscopy", 12.01 – 18.01.2013, Rehovot, Israel

DESY suvetudengite programm 2009, 21.07 – 10.09.2009, Hamburg, Saksamaa

# DISSERTATIONES PHYSICAE UNIVERSITATIS TARTUENSIS

1. **Andrus Ausmees.** XUV-induced electron emission and electron-phonon interaction in alkali halides. Tartu, 1991.
2. **Heiki Sõnajalg.** Shaping and recalling of light pulses by optical elements based on spectral hole burning. Tartu, 1991.
3. **Sergei Savihhin.** Ultrafast dynamics of F-centers and bound excitons from picosecond spectroscopy data. Tartu, 1991.
4. **Ergo Nõmmiste.** Leelishalogeniidide röntgenelektronemissioon kiiritamisel footonitega energiaga 70–140 eV. Tartu, 1991.
5. **Margus Rätsep.** Spectral gratings and their relaxation in some low-temperature impurity-doped glasses and crystals. Tartu, 1991.
6. **Tõnu Pullerits.** Primary energy transfer in photosynthesis. Model calculations. Tartu, 1991.
7. **Olev Saks.** Attoampri diapasoonis voolude mõõtmise füüsikalised alused. Tartu, 1991.
8. **Andres Virro.** AlGaAsSb/GaSb heterostructure injection lasers. Tartu, 1991.
9. **Hans Korge.** Investigation of negative point discharge in pure nitrogen at atmospheric pressure. Tartu, 1992.
10. **Jüri Maksimov.** Nonlinear generation of laser VUV radiation for high-resolution spectroscopy. Tartu, 1992.
11. **Mark Aizengendler.** Photostimulated transformation of aggregate defects and spectral hole burning in a neutron-irradiated sapphire. Tartu, 1992.
12. **Hele Siimon.** Atomic layer molecular beam epitaxy of $A^2B^6$ compounds described on the basis of kinetic equations model. Tartu, 1992.
13. **Tõnu Reinot.** The kinetics of polariton luminescence, energy transfer and relaxation in anthracene. Tartu, 1992.
14. **Toomas Rõõm.** Paramagnetic $H^{2-}$ and $F^+$ centers in CaO crystals: spectra, relaxation and recombination luminescence. Tallinn, 1993.
15. **Erko Jalviste.** Laser spectroscopy of some jet-cooled organic molecules. Tartu, 1993.
16. **Alvo Aabloo.** Studies of crystalline celluloses using potential energy calculations. Tartu, 1994.
17. **Peeter Paris.** Initiation of corona pulses. Tartu, 1994.
18. **Павел Рубин.** Локальные дефектные состояния в $CuO_2$ плоскостях высокотемпературных сверхпроводников. Тарту, 1994.
19. **Olavi Ollikainen.** Applications of persistent spectral hole burning in ultrafast optical neural networks, time-resolved spectroscopy and holographic interferometry. Tartu, 1996.
20. **Ülo Mets.** Methodological aspects of fluorescence correlation spectroscopy. Tartu, 1996.
21. **Mikhail Danilkin.** Interaction of intrinsic and impurity defects in CaS:Eu luminophors. Tartu, 1997.

22. **Ирина Кудрявцева.** Создание и стабилизация дефектов в кристаллах KBr, KCl, RbCl при облучении ВУФ-радиацией. Тарту, 1997.
23. **Andres Osvet.** Photochromic properties of radiation-induced defects in diamond. Tartu, 1998.
24. **Jüri Örd.** Classical and quantum aspects of geodesic multiplication. Tartu, 1998.
25. **Priit Sarv.** High resolution solid-state NMR studies of zeolites. Tartu, 1998.
26. **Сергей Долгов.** Электронные возбуждения и дефектообразование в некоторых оксидах металлов. Тарту, 1998.
27. **Kaupo Kukli.** Atomic layer deposition of artificially structured dielectric materials. Tartu, 1999.
28. **Ivo Heinmaa.** Nuclear resonance studies of local structure in $RBa_2Cu_3O_{6+x}$ compounds. Tartu, 1999.
29. **Aleksander Shelkan.** Hole states in $CuO_2$ planes of high temperature superconducting materials. Tartu, 1999.
30. **Dmitri Nevedrov.** Nonlinear effects in quantum lattices. Tartu, 1999.
31. **Rein Ruus.** Collapse of 3d (4f) orbitals in 2p (3d) excited configurations and its effect on the x-ray and electron spectra. Tartu, 1999.
32. **Valter Zazubovich.** Local relaxation in incommensurate and glassy solids studied by Spectral Hole Burning. Tartu, 1999.
33. **Indrek Reimand.** Picosecond dynamics of optical excitations in GaAs and other excitonic systems. Tartu, 2000.
34. **Vladimir Babin.** Spectroscopy of exciton states in some halide macro- and nanocrystals. Tartu, 2001.
35. **Toomas Plank.** Positive corona at combined DC and AC voltage. Tartu, 2001.
36. **Kristjan Leiger.** Pressure-induced effects in inhomogeneous spectra of doped solids. Tartu, 2002.
37. **Helle Kaasik.** Nonperturbative theory of multiphonon vibrational relaxation and nonradiative transitions. Tartu, 2002.
38. **Tõnu Laas.** Propagation of waves in curved spacetimes. Tartu, 2002.
39. **Rünno Lõhmus.** Application of novel hybrid methods in SPM studies of nanostructural materials. Tartu, 2002.
40. **Kaido Reivelt.** Optical implementation of propagation-invariant pulsed free-space wave fields. Tartu, 2003.
41. **Heiki Kasemägi.** The effect of nanoparticle additives on lithium-ion mobility in a polymer electrolyte. Tartu, 2003.
42. **Villu Repän.** Low current mode of negative corona. Tartu, 2004.
43. **Алексей Котлов.** Оксианионные диэлектрические кристаллы: зонная структура и электронные возбуждения. Tartu, 2004.
44. **Jaak Talts.** Continuous non-invasive blood pressure measurement: comparative and methodological studies of the differential servo-oscillometric method. Tartu, 2004.
45. **Margus Saal.** Studies of pre-big bang and braneworld cosmology. Tartu, 2004.

46. **Eduard Gerškevitš.** Dose to bone marrow and leukaemia risk in external beam radiotherapy of prostate cancer. Tartu, 2005.
47. **Sergey Shchemelyov.** Sum-frequency generation and multiphoton ionization in xenon under excitation by conical laser beams. Tartu, 2006.
48. **Valter Kiisk.** Optical investigation of metal-oxide thin films. Tartu, 2006.
49. **Jaan Aarik.** Atomic layer deposition of titanium, zirconium and hafnium dioxides: growth mechanisms and properties of thin films. Tartu, 2007.
50. **Astrid Rekker.** Colored-noise-controlled anomalous transport and phase transitions in complex systems. Tartu, 2007.
51. **Andres Punning.** Electromechanical characterization of ionic polymer-metal composite sensing actuators. Tartu, 2007.
52. **Indrek Jõgi.** Conduction mechanisms in thin atomic layer deposited films containing $TiO_2$. Tartu, 2007.
53. **Aleksei Krasnikov.** Luminescence and defects creation processes in lead tungstate crystals. Tartu, 2007.
54. **Küllike Rägo.** Superconducting properties of $MgB_2$ in a scenario with intra- and interband pairing channels. Tartu, 2008.
55. **Els Heinsalu.** Normal and anomalously slow diffusion under external fields. Tartu, 2008.
56. **Kuno Kooser.** Soft x-ray induced radiative and nonradiative core-hole decay processes in thin films and solids. Tartu, 2008.
57. **Vadim Boltrushko.** Theory of vibronic transitions with strong nonlinear vibronic interaction in solids. Tartu, 2008.
58. **Andi Hektor.** Neutrino Physics beyond the Standard Model. Tartu, 2008.
59. **Raavo Josepson.** Photoinduced field-assisted electron emission into gases. Tartu, 2008.
60. **Martti Pärs.** Study of spontaneous and photoinduced processes in molecular solids using high-resolution optical spectroscopy. Tartu, 2008.
61. **Kristjan Kannike.** Implications of neutrino masses. Tartu, 2008.
62. **Vigen Issahhanjan.** Hole and interstitial centres in radiation-resistant MgO single crystals. Tartu, 2008.
63. **Veera Krasnenko.** Computational modeling of fluorescent proteins. Tartu, 2008.
64. **Mait Müntel.** Detection of doubly charged higgs boson in the CMS detector. Tartu, 2008.
65. **Kalle Kepler.** Optimisation of patient doses and image quality in diagnostic radiology. Tartu, 2009.
66. **Jüri Raud.** Study of negative glow and positive column regions of capillary HF discharge. Tartu, 2009.
67. **Sven Lange.** Spectroscopic and phase-stabilisation properties of pure and rare-earth ions activated $ZrO_2$ and $HfO_2$. Tartu, 2010.
68. **Aarne Kasikov.** Optical characterization of inhomogeneous thin films. Tartu, 2010.
69. **Heli Valtna-Lukner.** Superluminally propagating localized optical pulses. Tartu, 2010.

70. **Artjom Vargunin.** Stochastic and deterministic features of ordering in the systems with a phase transition. Tartu, 2010.
71. **Hannes Liivat.** Probing new physics in e+e− annihilations into heavy particles via spin orientation effects. Tartu, 2010.
72. **Tanel Mullari.** On the second order relativistic deviation equation and its applications. Tartu, 2010.
73. **Aleksandr Lissovski.** Pulsed high-pressure discharge in argon: spectroscopic diagnostics, modeling and development. Tartu, 2010.
74. **Aile Tamm.** Atomic layer deposition of high-permittivity insulators from cyclopentadienyl-based precursors. Tartu, 2010.
75. **Janek Uin.** Electrical separation for generating standard aerosols in a wide particle size range. Tartu, 2011.
76. **Svetlana Ganina.** Hajusandmetega ülesanded kui üks võimalus füüsikaõppe efektiivsuse tõstmiseks. Tartu, 2011
77. **Joel Kuusk.** Measurement of top-of-canopy spectral reflectance of forests for developing vegetation radiative transfer models. Tartu, 2011.
78. **Raul Rammula**. Atomic layer deposition of $HfO_2$ – nucleation, growth and structure development of thin films. Tartu, 2011.
79. **Сергей Наконечный.** Исследование электронно-дырочных и интерстициал-вакансионных процессов в монокристаллах MgO и LiF методами термоактивационной спектроскопии. Тарту, 2011.
80. **Niina Voropajeva.** Elementary excitations near the boundary of a strongly correlated crystal. Tartu, 2011.
81. **Martin Timusk.** Development and characterization of hybrid electro-optical materials. Tartu, 2012, 106 p.
82. **Merle Lust.** Assessment of dose components to Estonian population. Tartu, 2012, 84 p.
83. **Karl Kruusamäe.** Deformation-dependent electrode impedance of ionic electromechanically active polymers. Tartu, 2012, 128 p.
84. **Liis Rebane.** Measurement of the $W \to \tau\nu$ cross section and a search for a doubly charged Higgs boson decaying to τ-leptons with the CMS detector. Tartu, 2012, 156 p.
85. **Jevgeni Šablonin.** Processes of structural defect creation in pure and doped MgO and NaCl single crystals under condition of low or super high density of electronic excitations. Tartu, 2013, 145 p.
86. **Riho Vendt**. Combined method for establishment and dissemination of the international temperature scale. Tartu, 2013, 108 p.
87. **Peeter Piksarv.** Spatiotemporal characterization of diffractive and non-diffractive light pulses. Tartu, 2013, 156 p.
88. **Anna Šugai.** Creation of structural defects under superhigh-dense irradiation of wide-gap metal oxides. Tartu, 2013, 108 p.
89. **Ivar Kuusik.** Soft X-ray spectroscopy of insulators. Tartu, 2013, 113 p.
90. **Viktor Vabson**. Measurement uncertainty in Estonian Standard Laboratory for Mass. Tartu, 2013, 134 p.

91. **Kaupo Voormansik.** X-band synthetic aperture radar applications for environmental monitoring. Tartu, 2014, 117 p.
92. **Deivid Pugal.** hp-FEM model of IPMC deformation. Tartu, 2014, 143 p.
93. **Siim Pikker.** Modification in the emission and spectral shape of photostable fluorophores by nanometallic structures. Tartu, 2014, 98 p.
94. **Mihkel Pajusalu**. Localized Photosynthetic Excitons. Tartu, 2014, 183 p.
95. **Taavi Vaikjärv.** Consideration of non-adiabaticity of the Pseudo-Jahn-Teller effect: contribution of phonons. Tartu, 2014, 129 p.
96. **Martin Vilbaste.** Uncertainty sources and analysis methods in realizing SI units of air humidity in Estonia. Tartu, 2014, 111 p.
97. **Mihkel Rähn.** Experimental nanophotonics: single-photon sources- and nanofiber-related studies. Tartu, 2015, 107 p.
98. **Raul Laasner.** Excited state dynamics under high excitation densities in tungstates. Tartu, 2015, 125 p.
99. **Andris Slavinskis.** EST Cube-1 attitude determination. Tartu, 2015, 104 p.
100. **Karlis Zalite**. Radar Remote Sensing for Monitoring Forest Floods and Agricultural Grasslands. Tartu, 2016, 124 p.
101. **Kaarel Piip.** Development of LIBS for *in-situ* study of ITER relevant materials. Tartu, 2016, 93 p.
102. **Kadri Isakar.** $^{210}$Pb in Estonian air: long term study of activity concentrations and origin of radioactive lead. Tartu, 2016, 107 p.
103. **Artur Tamm.** High entropy alloys: study of structural properties and irradiation response. Tartu, 2016, 115 p.
104. **Rasmus Talviste.** Atmospheric-pressure He plasma jet: effect of dielectric tube diameter. Tartu, 2016, 107 p.
105. **Andres Tiko.** Measurement of single top quark properties with the CMS detector. Tartu, 2016, 161 p.
106. **Aire Olesk.** Hemiboreal Forest Mapping with Interferometric Synthetic Aperture Radar. Tartu, 2016, 121 p.
107. **Fred Valk.** Nitrogen emission spectrum as a measure of electric field strength in low-temperature gas discharges. Tartu, 2016, 149 p.
108. **Manoop Chenchiliyan.** Nano-structural Constraints for the Picosecond Excitation Energy Migration and Trapping in Photosynthetic Membranes of Bacteria. Tartu, 2016, 115p.
109. **Lauri Kaldamäe.** Fermion mass and spin polarisation effects in top quark pair production and the decay of the higgs boson. Tartu, 2017, 104 p.